

FMR-related phenomena in spintronic devices

Yi Wang, Rajagopalan Ramaswamy, and Hyunsoo Yang

Department of Electrical and Computer Engineering, National University of Singapore, 117576, Singapore

Spintronic devices, such as non-volatile magnetic random access memories and logic devices, have attracted considerable attention as potential candidates for future high efficient data storage and computing technology. In a heavy metal or other emerging material with strong spin-orbit coupling (SOC), the charge currents induce spin currents or spin accumulations via SOC. The generated spin currents can exert spin-orbit torques (SOTs) on an adjacent ferromagnet, which opens up a new way to realize magnetization dynamics and switching of the ferromagnetic layer for spintronic devices. In the SOT scheme, the charge-to-spin interconversion efficiency (SOT efficiency) is an important figure of merit for applications. For the effective characterization of this efficiency, the ferromagnetic resonance (FMR) based methods, such as the spin transfer torque ferromagnetic resonance (ST-FMR) and the spin pumping, are common utilized in addition to low frequency harmonic or dc measurements. In this review, we focus on the ST-FMR measurements for the evaluation of the SOT efficiency. We provide a brief summary of the different ST-FMR setups and data analysis methods. We then discuss ST-FMR and SOT studies in various materials, including heavy metals and alloys, topological insulators, two dimensional (2D) materials, interfaces with strong Rashba effect, antiferromagnetic materials, two dimensional electron gas (2DEG) in oxide materials and oxidized nonmagnetic materials.

Keywords: magnetization dynamics, spin transfer torque ferromagnetic resonance, spin-orbit torque efficiency, charge-to-spin current conversion

CONTENTS

1. Introduction	3
2. Magnetization dynamics	4
2.1. LLG equation	4
2.2. Ferromagnetic resonance (FMR)	5
2.3. Spin transfer torque ferromagnetic resonance (ST-FMR)	6
3. ST-FMR setups	8
3.1. Traditional ST-FMR setup with a dc voltmeter	8
3.2. Precise ST-FMR setup with a lock-in amplifier	9
3.3. Design of CPW and impedance match	11
4. Methods to evaluate the spin-orbit torque (SOT) and SOT efficiency	12
4.1. Ratio of V_S/V_A	13
4.2. Only- V_S	14
4.3. Modulation of damping (MOD)	15
5. Spin Hall effect (SHE) in heavy metals and alloys	17
5.1. Spin Hall effect in Pt	19
5.2. Spin Hall effect in Ta	23
5.3. Spin Hall effect in tungsten (W) and other alloys with heavy metal dopants	26
5.4. Role of interface transparency of HM and FM in the SOT efficiency	28
5.5. Difference in the SOT efficiency between ST-FMR and magnetization switching technique	30
6. SOT in topological insulators (TIs)	31
6.1. SOT efficiency in TIs	33
6.2. Anisotropic SOT (efficiency) in Bi_2Se_3 MBE films	35
6.3. TSS dominated SOT	38
7. SOT beyond HMs and TIs	40
7.1. Interface between two nonmagnetic materials	41
7.2. Transition-metal dichalcogenides (TMDs)	44
7.3. Antiferromagnetic (AFM) materials	46
7.4. 2DEG in oxide materials	48
7.5. Nonmagnetic oxidized materials	50
8. Summary and Perspectives	51
Acknowledgments	56
References	57

1. Introduction

In the recent years, the electrical manipulation of the magnetization is a central theme for modern spintronics [1-3]. Following the successful applications of magnetic tunnel junctions (MTJs) [4, 5] in the read heads of hard disk drives, new functional spintronic devices, such as non-volatile magnetic random access memories (MRAM) and magnetic logic devices [6, 7], are being pursued enthusiastically by researchers nowadays. For practical spintronic applications, it is desired to achieve efficient magnetization manipulation via electrical means with a higher operation speed and lower energy consumption. In order to evaluate the efficiency of the electrical manipulation of the magnetization as well as to understand underlying physics in the magnetic devices, various techniques based on magnetization dynamics under application of currents have been developed.

The study of magnetization dynamics can be dated back to the observation of ferromagnetic resonance (FMR) in the first half of the 20th century [8, 9]. Originally, FMR was used to study magnetic films and the magnetization dynamics in such films in the context of external magnetic fields only. With the discovery of spin transfer torques (STT) in the year 1996 [10, 11] and development of the modern nano-fabrication techniques which allow the device dimensions to be scaled-down, electrical manipulation of nanomagnets using spin-polarized current injection gained popularity. After the year 2000, the STT driven magnetization switching using electric currents was experimentally observed in giant magnetoresistance (GMR) nanopillars and nanosized MTJ devices [12-14]. In order to get insight into the magnetization dynamics of an individual nanomagnet or magnetic device under the application of an electric current, the spin transfer torque ferromagnetic resonance (ST-FMR) technique was developed and explored in GMR nanopillars and nanosized MTJs [15-18].

One of the drawbacks of the STT scheme is the requirement of an additional magnet to create spin polarized currents. In the year 2004, the imaging of direct charge-to-spin current conversion in a single semiconductor GaAs due to the spin Hall effect (SHE) was observed [19]. Ever since this observations, pure spin current generation in non-magnets has drawn tremendous attention for spintronic devices [2]. Recently, it was demonstrated that the magnetization can be switched or driven into precession modes by only pure spin currents [20-24], which opened up a new route to realize spintronic devices. In order to achieve highly efficient magnetization manipulation, a key challenge is to identify materials that exhibit a large charge-to-spin interconversion efficiency (i.e. spin Hall angle or spin-orbit torque efficiency). The ST-FMR is an effective technique to evaluate the spin-orbit torque (SOT) efficiency. The first demonstration was reported in a Pt/NiFe bilayer planar spin Hall device in 2011 [25], which is based on the spin rectification of the anisotropic magnetoresistance (AMR) effect. Subsequently, ST-FMR has been used to evaluate the SOT efficiencies and understand the underlying physics in many emerging materials as presented later on.

This article provides a topical review of ST-FMR technique and its applications in studying the SOT related phenomena in diverse emerging materials. In Section 2, we begin with the basic principle of magnetization dynamics. In Section 3 and 4, we introduce the ST-FMR setups and data analysis methods. In Section 5, 6 and 7, we review the progress in the SOT studies by using ST-FMR technique in different material systems, such as heavy metals, topological insulators and other emerging material systems, and we end with a summary and perspectives in Section 8.

2. Magnetization dynamics

2.1. LLG equation

Under macrospin approximation, the time domain dynamics of the magnetization vector (\mathbf{m})

of a ferromagnet in the presence of an effective magnetic field (\mathbf{H}_{eff}) can be described by the Landau-Lifshitz-Gilbert (LLG) equation [26],

$$\frac{\partial \mathbf{m}}{\partial t} = (-\gamma \mu_0 \mathbf{m} \times \mathbf{H}_{\text{eff}}) + \left(\alpha \mathbf{m} \times \frac{\partial \mathbf{m}}{\partial t} \right) \quad (1)$$

where γ , μ_0 , and α are the gyromagnetic ratio, vacuum permeability, the Gilbert damping parameter, respectively. The right hand side of the LLG equation has two torque terms – the first term, $-\gamma \mu_0 \mathbf{m} \times \mathbf{H}_{\text{eff}}$, is a precession term that rotates \mathbf{m} around \mathbf{H}_{eff} , while the second term, $\alpha \mathbf{m} \times \frac{\partial \mathbf{m}}{\partial t}$, is the damping (or energy dissipation) term which aligns \mathbf{m} along \mathbf{H}_{eff} . The value of α determines the rate at which \mathbf{m} damps towards the \mathbf{H}_{eff} . When the value of α is large (small), \mathbf{m} damps towards \mathbf{H}_{eff} at a faster (slower) rate.

When a spin polarized current (polarized along $\hat{\sigma}$) interacts with \mathbf{m} , there are additional torques experienced by \mathbf{m} and the LLG equation is modified as [10, 11, 27]

$$\frac{\partial \mathbf{m}}{\partial t} = -\gamma \mu_0 \mathbf{m} \times \mathbf{H}_{\text{eff}} + \alpha \mathbf{m} \times \frac{\partial \mathbf{m}}{\partial t} + \boldsymbol{\tau}_{\text{DL}} + \boldsymbol{\tau}_{\text{FL}} \quad (2)$$

where $\boldsymbol{\tau}_{\text{DL}}$ is of the $\mathbf{m} \times (\hat{\sigma} \times \mathbf{m})$ symmetry and is called the damping-like torque, while $\boldsymbol{\tau}_{\text{FL}}$ is of the $\hat{\sigma} \times \mathbf{m}$ symmetry and is called the field-like torque.

2.2. Ferromagnetic resonance (FMR)

In Section 2.1, it was discussed that in the presence of \mathbf{H}_{eff} , \mathbf{m} precesses about \mathbf{H}_{eff} . Due to energy dissipation (damping) in the ferromagnet, the amplitude of these precessions continuously decays. An external energy supplied to the ferromagnet in the form of an alternating magnetic field (H_{RF}) can compensate this energy dissipation leading to forced precession of \mathbf{m} . If the frequency of H_{RF} is tuned to the natural precession frequency of \mathbf{m} , the amplitude of the forced precession will be maximum due to resonance. This resonance is called the ferromagnetic resonance and the

precession frequency during the resonance condition is called the resonance frequency ($f = \omega_{\text{res}}/2\pi$).

f and H_0 (the resonant field) are related by the Kittel's relation,

$$f = (\gamma/2\pi)[H_0(H_0 + 4\pi M_{\text{eff}})]^{1/2} \quad (3)$$

where $4\pi M_{\text{eff}}$ is the effective demagnetization field of the ferromagnet. According to equation (3), the resonance condition can be matched by fixing H_0 and tuning the frequency of H_{RF} or vice versa.

2.3. Spin transfer torque ferromagnetic resonance (ST-FMR)

In contrast to the magnetic field driven FMR, it is possible to excite FMR using spin torques generated by an alternating current, called ST-FMR. The ST-FMR technique was first used in a Pt/NiFe (Py) bilayer in the case of a spin Hall scheme [25], which is proved to be an effective method to evaluate the charge-to-spin conversion efficiency (i.e. spin Hall angle). We first provide a more general description of ST-FMR process in the Pt/Py bilayer as an example.

As shown in figure 1(a), when an in-plane rf charge current (I_{RF}) is injected into the Pt/Py bilayer, non-equilibrium spins are generated at the Pt/Py interface due to the spin-orbit coupling (SOC) in the Pt layer. Subsequently, these generated spins diffuse into the adjacent Py layer and exert SOTs (damping-like torque, τ_{DL} and/or field-like torque, τ_{FL}) on the Py local magnetization. In addition, the current in the Pt layer induced Oersted field can also exert the Oersted field torque (τ_{Oe}) on the Py magnetization. Since the injected charge current is oscillatory, all the above torques are oscillatory and hence trigger the Py magnetization into precession around the direction of effective magnetic field, which leads to an oscillatory AMR in the ST-FMR device. Consequently, the oscillation of the AMR and the I_{RF} in the ST-FMR device produce a mixing ST-FMR voltage V_{mix} across the Pt/Py bilayer, which can be detected by a dc voltmeter or a lock-in amplifier. Since the ST-FMR signal is the spin rectification of the magnetoresistance in the device [28], the ST-FMR technique has a high enough sensitivity and can be used to study the micro-sized or even

nanosized magnetic devices.

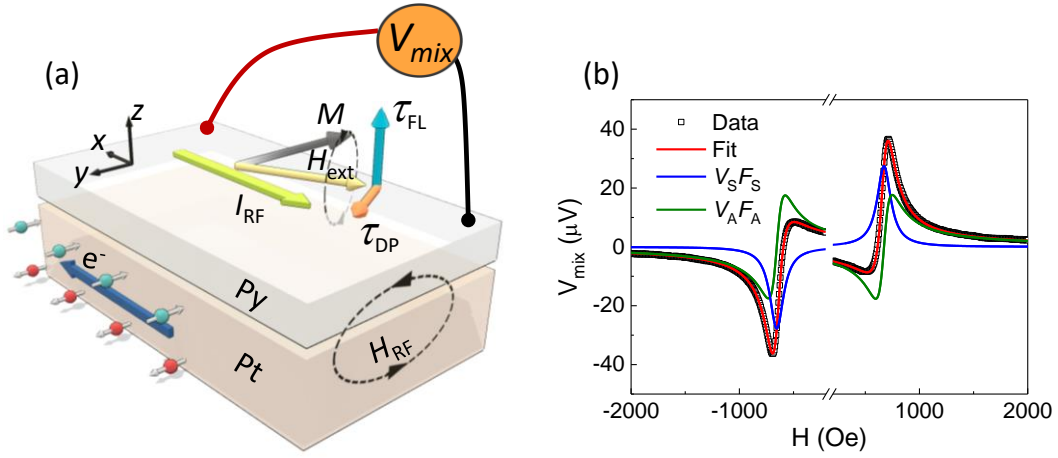


Figure 1. (a) Illustration of spin current generation in Pt and SOT driven Py magnetization dynamics in the ST-FMR measurements. The big blue arrow denotes the electron flow direction (opposite to the I_{RF} direction). The blue with green and red balls denote the generated spin polarizations in the Pt layer. (b) A typical ST-FMR signal (open symbols) from a Pt (6 nm)/Py (4 nm) device at 6 GHz with fits (solid curves), where the blue and green curves represent the symmetric Lorentzian ($V_S F_S$) and antisymmetric Lorentzian ($V_A F_A$) components, respectively.

Subsequently, we present a derivation of general expression for the ST-FMR signal V_{mix} . The applied rf current to the Pt/Py ST-FMR device is written as $I_{RF} = I \cos(\omega t)$, where I is the amplitude of I_{RF} with a frequency of $\omega/2\pi$. The device resistance is $R(t) = R_0 + \Delta R \cos^2 \theta(t)$, where R_0 is the resistance when I_{RF} is perpendicular to the Py magnetization direction, ΔR is the AMR. $\theta(t)$ is the angle between I_{RF} and Py magnetization, which is a function of time t due to magnetization precession, given by the equation $\theta(t) = \theta_H + \theta_c \cos(\omega t + \delta)$, where θ_H is the constant angle between H_{ext} and I_{RF} , θ_c is the cone angle of Py magnetization precession, which is a measure of the total torques on the Py magnetization. Usually, θ_c is much smaller than θ_H . δ is the resonance phase between the driven force (i.e. damping-like torque τ_{DL} , field-like torque τ_{FL} or Oersted field torque τ_{Oe}) and the magnetization response (i.e. the oscillation of AMR) [29, 30].

By using the Taylor's expansion, we get $\cos\theta(t) = \cos\theta_H - \sin\theta_H \cdot \theta_c \cos(\omega t + \delta)$ and $R(t) = R_0 + \Delta R[\cos^2\theta_H - 2\cos\theta_H \sin\theta_H \cdot \theta_c \cos(\omega t + \delta)]$. Hence, the product is

$$\begin{aligned} V(t) &= I(t)R(t) \\ &= (IR_0 + I\Delta R \cos^2\theta_H)\cos(\omega t) - I\Delta R \sin(2\theta_H) \cdot \theta_c \cos(2\omega t + \delta)/2 \\ &\quad - I\Delta R \sin(2\theta_H) \cdot \theta_c (\cos\delta)/2 \end{aligned}$$

The total voltage $V(t)$ comprises of three terms at frequencies ω , 2ω , and a time-independent term.

The last dc term is the rectified ST-FMR signal, $V_{\text{mix}} = -I\Delta R \sin(2\theta_H) \cdot \theta_c (\cos\delta)/2$. The ST-FMR signal is determined by the combination of the amplitude of I_{RF} , AMR in the device, the angle of H_{ext} with respect to I_{RF} , the cone angle of magnetization precession θ_c and the resonance phase δ .

For an in-plane alternative magnetic field driven magnetization dynamics of an in-plane magnetization [30, 31], the value of δ changes from π to 0 around the resonance field H_0 with a linewidth of ΔH (full width at half maximum) and $\delta = \pi/2$ at the resonance field H_0 . Therefore, the V_{mix} attributed to the in-plane alternative magnetic field has an antisymmetric Lorentzian line shape, which is the case for the τ_{Oe} and/or τ_{FL} driven magnetization dynamics in a Pt/Py ST-FMR device as shown by the green curves in figure 1(b). Whereas for the τ_{DL} driven magnetization dynamics, there is an additional 90° phase difference compared to τ_{FL} or τ_{Oe} driven magnetization dynamics for an AMR based rectification system. Therefore, the driving force τ_{DL} is in-phase ($\delta = 0$) at the resonance field H_0 , leading to a symmetric Lorentzian line shape arising from the damping-like torque in a Pt/Py ST-FMR device as illustrated by the blue curves in figure 1(b). In Section 4, we will present three quantitative analyses of the ST-FMR signal in detail.

3. ST-FMR setups

3.1. Traditional ST-FMR setup with a dc voltmeter

As described in Section 2.3, the ST-FMR signal is a rectified dc voltage, which can be detected

directly by a dc voltmeter. Figure 2 shows a schematic of the traditional ST-FMR setup with a dc voltmeter. It depicts a typical ST-FMR device with a micro-strip of heavy metal (HM)/ferromagnet (FM) bilayer structure. A ground-signal-ground (G-S-G) coplanar waveguide (CPW) is fabricated with one G and one S electrodes contacting the HM/FM bilayer channel for applying an I_{RF} to the ST-FMR device which is supplied by a signal generator (SG) connected to an rf port of a bias tee. A ST-FMR signal can be simultaneously detected by a voltmeter, such as Keithley 2182A and Keithley 2002, connected to the low frequency port of the bias tee as shown in the figure 2. The traditional ST-FMR setup with a dc voltmeter usually works well for the devices having considerable amplitude of ST-FMR signals with the value of several tens of μV , such as Pt/Py systems [25, 32].

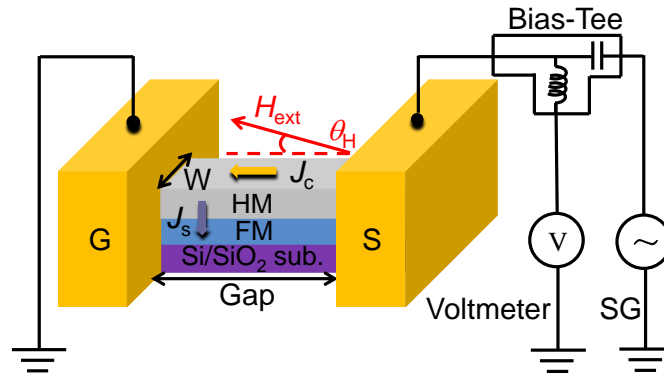


Figure 2. The schematic of the traditional ST-FMR measurement setup, illustrating the ST-FMR device and measurement circuit including a bias tee, a high frequency signal generator and a dc voltmeter. Adapted from [32], with the permission of AIP Publishing.

3.2. Precise ST-FMR setup with a lock-in amplifier

For the traditional ST-FMR setup, the noise level is usually in the order of ~ 100 nV because of the limitation of a dc voltmeter. This noise level reduces the signal-to-noise ratio substantially while studying some of the emerging material systems possessing smaller ST-FMR signals with the order of $\sim \mu\text{V}$, such as the topological insulator/FM bilayers [33, 34]. In order to decrease the noise (i.e., increase the signal-to-noise ratio), a more sensitive ST-FMR setup was developed in

which the dc voltmeter is replaced with a lock-in amplifier [16, 35]. Figure 3(a) shows the ST-FMR setup with lock-in technique.

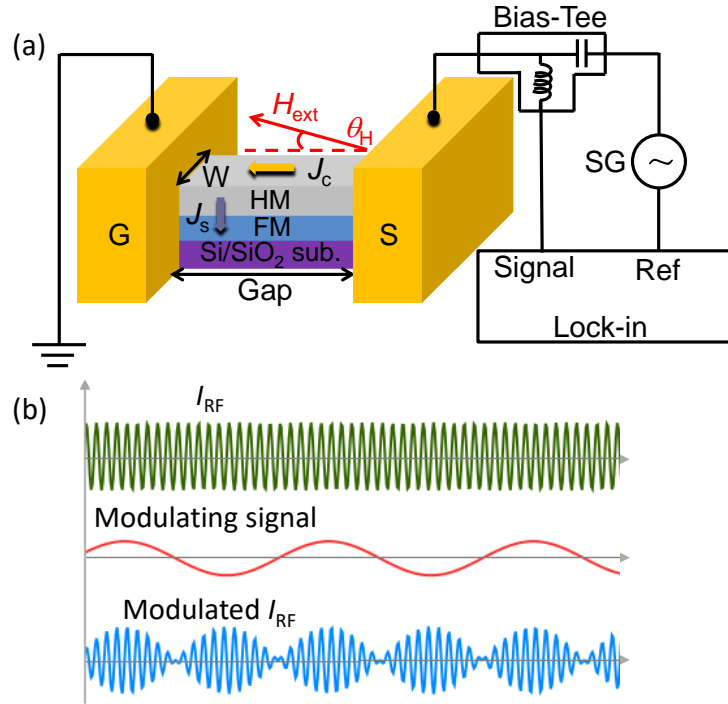


Figure 3. (a) The schematic of the sensitive ST-FMR setup with a lock-in amplifier, illustrating the ST-FMR device and measurement circuit including a bias tee, a high frequency signal generator and a lock-in amplifier. Adapted from [32], with the permission of AIP Publishing. (b) Illustration of the amplitude modulation of input I_{RF} from a signal generator by a modulating signal with a much lower frequency, and the modulated I_{RF} is finally injected into the ST-FMR device.

The input I_{RF} is amplitude modulated by a low frequency sinusoidal wave signal (modulating signal) as illustrated in figure 3(b). The low frequency modulating signal is also provided as a reference signal into the reference port of the lock-in amplifier and thus serves as a trigger. The modulated I_{RF} is injected into the ST-FMR device to give rise to the ST-FMR signal. The ST-FMR signal, in this case, is a low frequency voltage (instead of a dc) since the I_{RF} is amplitude modulated. The low frequency ST-FMR signal can be detected by the lock-in amplifier with the phase locking technique. Therefore, the noise level can be less than ~ 10 nV, thus providing a better signal-to-noise ratio compared to the traditional ST-FMR setup.

3.3. Design of CPW and impedance match

In order to avoid a large amount of rf power loss or reflection during the rf current transmission in the CPW and the HM/FM current channel, the ST-FMR device should be designed to have an impedance (Z_m) of around 50Ω . First, the CPW should be designed considering impedance matching. One example of a typical CPW is illustrated in figure 4(a). The width of S is s and the gap between S and G line is w . The characteristic impedance of the CPW can be tuned by varying the s and/or w values. One can use a common CPW calculator software to select the proper combination of s and w values for the CPW design. For example, the s is about $60 \mu\text{m}$ and w is about $30 \mu\text{m}$ for the CPW design in Ref. [32]. Further, the HM/FM bilayer current channel should also be impedance matched, which can be tuned by changing the channel length L and width W (also see the current channel denoted by the red circles in the figures 4(b) and (c)). For example, L is in the range of $\sim 10 - 60 \mu\text{m}$ and W is in the range of $\sim 10 - 30 \mu\text{m}$ in Refs. [32-34]. Finally, Z_m of ST-FMR devices can be quantitatively calibrated by the microwave-network-analysis measurement using a vector network analyzer (VNA).

Usually, there are two kinds of CPW designs, namely the asymmetric and the symmetric CPW designs. The asymmetric CPW design is shown in figure 4(b), which was initially used for the HM/FM bilayer ST-FMR measurements [25]. However, there is a limitation of the asymmetric CPW. To elaborate on this limitation, consider the example of Pt/Py ST-FMR device as shown in figure 4(d). In addition to the current induced in-plane Oersted field (H_{RF}) to the Py magnetization, an imbalanced current induced out-of-plane Oersted field H_z from the contacting electrodes can be produced as I_{RF} is transmitting along the CPW [32, 36]. Consequently, H_z exerts an in-plane torque ($-m \times H_z$) on the Py magnetization and generates symmetric voltage signals for both directions of H_{ext} , which superimpose onto the symmetric signals arising from damping-like torque, τ_{DL} , from

spin currents. Therefore, the H_z induced torque might lead to an overestimation or underestimation of the spin Hall angle in Pt. However, one can eliminate this contamination by carefully locating the GSG probe position in the middle of the CPW [32].

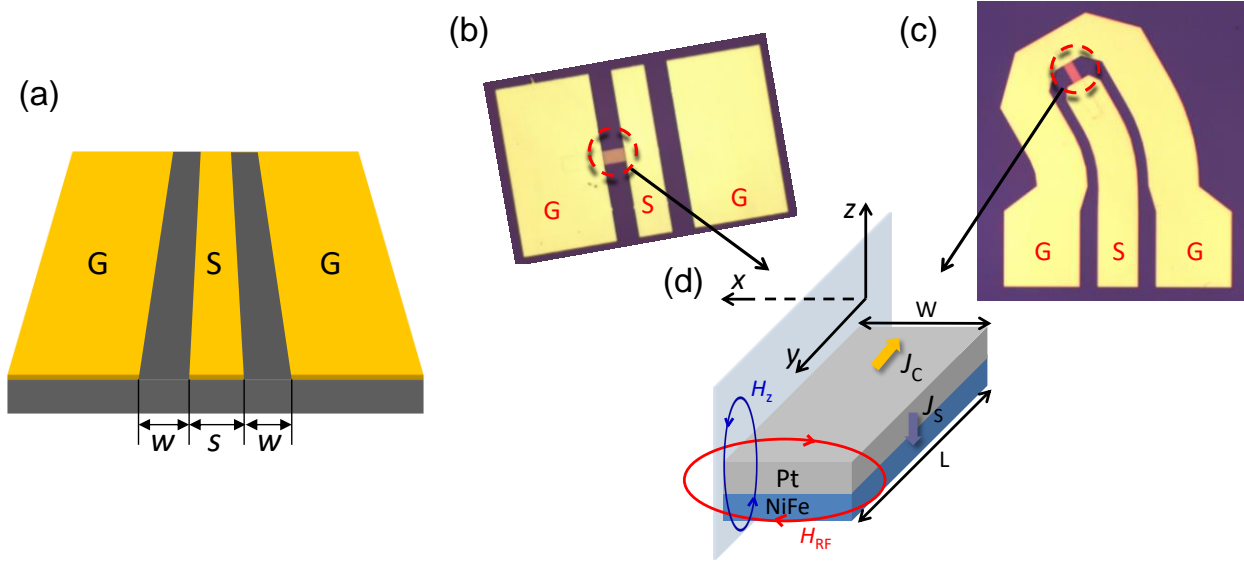


Figure 4. (a) The schematic of a typical CPW, illustrating the ground-signal-ground (G-S-G) transmission line. ST-FMR devices with (b) asymmetric CPW and (c) symmetric CPW. (d) The Pt/Py microstrip with the charge current J_C , spin current J_S , current induced in-plane Oersted field (H_{RF}). H_z is the current induced imbalanced out-of-plane Oersted field in the ST-FMR device with asymmetric CPW design. Adapted from [32], with the permission of AIP Publishing.

In order to diminish or eliminate the imbalanced H_z and the related influences in the ST-FMR measurements and spin Hall angle evaluation, the symmetric CPW design was developed. As shown in figure 4(c), the current induced Oersted field in the electrodes is balanced as I_{RF} flows in the symmetric CPW, resulting in no H_z component. Therefore, the symmetric CPW design is better than the asymmetric CPW for ST-FMR measurements.

4. Methods to evaluate the spin-orbit torque (SOT) and SOT efficiency

In Section 2.3, a general derivation of ST-FMR signal was provided. In this section, we will further present three quantitative analyses of the ST-FMR signal. The ST-FMR signals from a HM/FM bilayer device (see figure 1(b)) can be fitted by $V_{\text{mix}} = V_S F_S(H_{\text{ext}}) + V_A F_A(H_{\text{ext}})$, where

$F_S(H_{\text{ext}}) = \Delta H^2 / [(H_{\text{ext}} - H_0)^2 + \Delta H^2]$ is a symmetric Lorentzian function of amplitude V_S and $F_A(H_{\text{ext}}) = \Delta H(H_{\text{ext}} - H_0) / [(H_{\text{ext}} - H_0)^2 + \Delta H^2]$ is an antisymmetric Lorentzian function of amplitude V_A [25, 32]. The symmetric component has a maximum value at the resonance field H_0 and is centered about H_0 , whereas, the antisymmetric component has a dispersive curve with the value of zero at H_0 . Both components have the same linewidth ΔH with respect to the magnetic field.

4.1. Ratio of V_S/V_A

It is noted that V_S is proportional to the amplitude of spin currents J_S (i.e. τ_{DL}) and is written as $V_S \propto \hbar J_S / (2e\mu_0 M_s t)$ [18, 25, 37], where M_s and t are the saturation magnetization and thickness of the FM layer, respectively, and \hbar is the reduced Planck constant. While V_A is correlated with H_{RF} induced Oersted field torque (τ_{Oe}), which is written as $V_A \propto H_{RF} [1 + (4\pi M_{\text{eff}} / H_{\text{ext}})]^{1/2}$ [18, 25, 37], where M_{eff} is the effective magnetization of the FM layer. Note that the field-like torque τ_{FL} is assumed to be negligible here. H_{RF} is estimated by Ampere's law as $H_{RF} = J_C d / 2$, where J_C is the charge current density in the HM layer. Note that the charge current flowing in the FM layer is assumed to be spatially uniform, therefore, there is no net Oersted field torque on the FM magnetization itself.

In the spin Hall scheme, the charge-to-spin conversion efficiency (i.e. spin Hall angle), defined as $\theta_{\text{sh}} = J_S / J_C$, can be found from the ratio of V_S/V_A [25]. Using the above equations, one obtains the spin Hall angle as $\theta_{\text{sh}} = (V_S/V_A)(e\mu_0 M_s t d / \hbar) [1 + (4\pi M_{\text{eff}} / H_{\text{ext}})]^{1/2}$. This method is self-calibrated in the sense that the torques on the FM magnetization only arise from J_C in the Pt layer and the spin Hall angle can be easily calculated without knowing the exact values of I_{RF} and H_{RF} in ST-FMR devices. The method works well to determine θ_{sh} under the assumption that the V_A

only attributes to H_{RF} . In other words, this method may give rise to a wrong estimate of θ_{sh} for the case of a non-negligible field-like torque τ_{FL} , which might arise due to the interfacial effects, such as the Rashba effect. Since τ_{FL} can also produce an antisymmetric Lorentzian line shape signal similar to H_{RF} , the value of θ_{sh} might be overestimated or underestimated from the method of $V_{\text{S}}/V_{\text{A}}$ [38, 39]. Therefore, one should be aware of no significant field-like torque from interfacial effect before using the analysis method of the ratio of $V_{\text{S}}/V_{\text{A}}$.

Note that for simplicity, hereafter, we refer the spin Hall angle as the SOT efficiency, unless otherwise specified, in order to represent the charge-to-spin conversion efficiency in a variety of materials. After obtaining the SOT efficiency, we can easily evaluate the damping-like torque using $\tau_{\text{DL}} = \theta_{\text{sh}} J_{\text{C}} \hbar / (2e M_{\text{s}} t)$.

4.2. Only- V_{S}

Since some material systems give rise to a significant τ_{FL} to the adjacent FM magnetization, the SOT efficiency can be better determined by analyzing the symmetric component V_{S} only [33, 34, 40]. The damping like torque, τ_{DL} , and the associated in-plane SOT efficiency, θ_{sh} , can be evaluated using $V_{\text{S}} = -\frac{I_{\text{RF}} \gamma \cos \theta_{\text{H}}}{4} \frac{dR}{d\theta_{\text{H}}} \tau_{\text{DL}} \frac{1}{\Delta} F_{\text{S}}(H_{\text{ext}})$, $\sigma_{\text{S}} = J_{\text{S}}/E = \tau_{\text{DL}} M_{\text{s}} t/E$, and $\theta_{\text{sh}} = \sigma_{\text{S}}/\sigma$

[33, 34, 40], where $dR/d\theta_{\text{H}}$ is the angular dependent magnetoresistance at θ_{H} , Δ is the linewidth of ST-FMR signal in the frequency domain, E is the microwave electric field across the ST-FMR device, and σ_{S} and σ are the spin Hall and longitudinal charge conductivities of the HM layer, respectively. In addition, the field-like torque, τ_{FL} , can be derived by

$$V_{\text{A}} = -\frac{I_{\text{rf}} \gamma \cos \theta_{\text{H}}}{4} \frac{dR}{d\theta_{\text{H}}} (\tau_{\text{FL}} + \tau_{\text{Oe}}) \frac{[1 + (\mu_0 M_{\text{eff}}/H_{\text{ext}})]^{1/2}}{\Delta} F_{\text{asym}}(H_{\text{ext}}) \quad [33, 40].$$

In order to obtain τ_{FL} , the τ_{Oe} should be evaluated separately and excluded [33]. Similarly, the out-of-plane SOT

efficiency, θ_{\perp} , can be evaluated accordingly.

Since the resistance of the HM/FM microstrip is written as $R = R_0 + \Delta R \cos^2(\theta_H)$ due to the AMR effect (see Section 2.3), we obtain $\frac{dR}{d\theta_H} = -2\Delta R \sin(\theta_H)\cos(\theta_H) \propto \sin(\theta_H)\cos(\theta_H)$.

Consequently, we find $V_{\text{mix}} \propto \cos^2(\theta_H)\sin(\theta_H)$ from the relation, $V_{\text{mix}} \propto \frac{dR}{d\theta_H} \cos(\theta_H)$ [32]. Thus, it is observed that even though the change of AMR is maximum at $\theta_H = 45^\circ$, the largest ST-FMR signals are achieved at $\theta_H \sim 35^\circ$.

The comparison of the in-plane SOT efficiencies evaluated from the ratio of V_S/V_A method and from only- V_S method is presented in Section 5.1 for Pt and Section 5.2 for Ta. These results suggest that the only- V_S method is a more general way to evaluate the SOT efficiency in materials with SOC. However, compared to the V_S/V_A ratio method, the only- V_S technique requires additional measurements to determine the $dR/d\theta_H$ and σ , and also requires quantitative determination of I_{RF} through a ST-FMR device by considering the device impedance and rf power losses using the microwave-network analysis measurement [32].

Note that the SOT efficiency or in-plane SOT efficiency in the entire review for a variety of materials is denoted as θ_{sh} , and the out-of-plane SOT efficiency is denoted as θ_{\perp} , in order to be consistent.

4.3. Modulation of damping (MOD)

In the context of conventional STT, researchers found that the STT and magnetization fluctuation can be modulated in the vertical MTJs by applying a dc current bias [41, 42]. Recently, this method was used for HM/FM bilayer systems in the spin Hall scheme and the magnetization dynamics can be tuned by applying a dc current in the HM layer [43]. Based on the STT theory

[41], the effective magnetic damping (α) and thus the FMR linewidth (ΔH) will increase or decrease depending on the relative direction of spin polarizations with respect to the magnetization direction. The relationship can be written as [25]

$$\Delta H = (\Delta H)_0 + (\Delta H)_{\text{sh}} = \frac{2\pi f}{\gamma} \alpha + \frac{2\pi f}{\gamma} \frac{\sin \theta_H}{(H_{\text{ext}} + 2\pi M_{\text{eff}}) \mu_0 M_s t} \frac{\hbar}{2e} J_C \theta_{\text{sh}},$$

where $(\Delta H)_0$ is the linewidth at zero dc bias, $(\Delta H)_{\text{sh}}$ is the modulated linewidth due to the dc bias induced spin currents, and f is the rf current frequency. Therefore, one can perform the ST-FMR measurements to extract the ΔH as a function of J_C as shown in figure 5. By linearly fitting the data, the SOT efficiency is obtained accordingly.

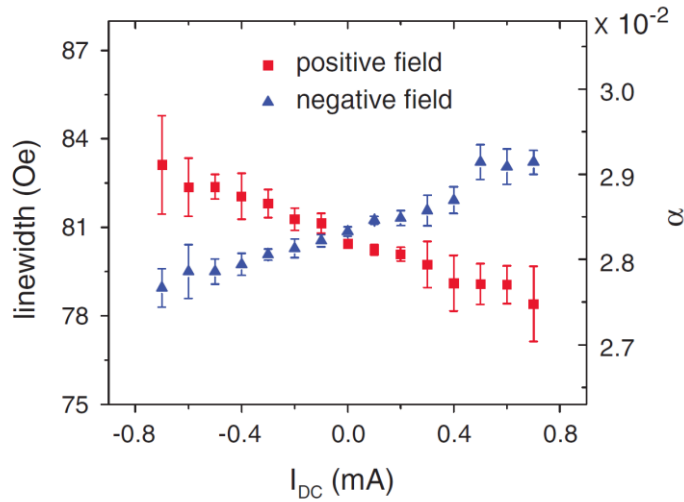


Figure 5. The FMR linewidth and Gilbert damping coefficient α as a function of dc current, I_{dc} , in the Pt (6 nm)/Py (4 nm) bilayer device at $f = 8$ GHz. Reprinted with permission from [25]. Copyright (2011) by the American Physical Society.

The modulation of damping (MOD) method is an extension of the ST-FMR measurements. So far, it has been used to evaluate the SOT efficiency commonly in Pt and Ta [25, 44-47], which usually have considerably large ST-FMR signals. Recently, it has been utilized for the SOT efficiency evaluation of metallic antiferromagnetic materials [48]. However, for the material

systems possessing smaller ST-FMR signals, it is challenging to employ the MOD method to evaluate the SOT efficiency [40].

Table 1 summarizes the advantages and disadvantages of the above three SOT efficiency evaluation methods. The method of V_S/V_A is simple, however it works only for the material systems where the V_A only attributes to H_{RF} (i.e. there is no significant field-like torque). Therefore, this method has limitations for the SOT efficiency evaluation. However, the method of only- V_S can successfully address this issue and can be a more general method to extract the SOT efficiency in a wide range of materials.

Methods	V_S/V_A	MOD	Only- V_S
Parameters required to estimate θ_{sh}	$V_S, V_A, M_s, t, d, M_{eff}$ and H_{ext}	$(\Delta H)_{sh, f}, \theta_H, H_{ext}, M_s, t, M_{eff}$, and J_C	$V_S, I_{RF}, \theta_H, dR/d\theta_H, \Delta, M_s, t, E$ and σ
Analysis procedure	Can directly get θ_{sh} from ST-FMR lineshape analysis	Needs precise ST-FMR linewidth measurements and analysis	Needs additional AMR ($dR/d\theta_H$), conductivity (σ) measurements and rf power analysis
Material systems	Limited to material systems without significant τ_{FL}	Material systems with considerably large and clean ST-FMR signals	Almost all material systems showing ST-FMR signals
Remarks	A simple method but with serious limitations	A less simple method but with moderate limitations	A more general method, but need extra measured parameters
References	[25], [32]	[25], [44-48]	[32-34], [40]

Table 1. Summary of the advantages and disadvantages of three SOT efficiency evaluation methods.

5. Spin Hall effect (SHE) in heavy metals and alloys

Spin Hall effect [49-52] is an electrical technique, which exploits the bulk SOC in a nonmagnetic material (such as HM) to convert charge currents into pure spin currents without any

external magnetic field. The first theoretical predictions of SHE by Dyakonov and Perel dates back to 1971 [53] and, in 1999, the SHE method to generate spin currents was reinvigorated by Hirsch [49]. Subsequently, in 2004, the SHE was first experimentally observed in the GaAs system [19]. The phenomenon of SHE relies on the spin-dependent asymmetric scattering of the unpolarized electrons due to the bulk SOC in the nonmagnetic materials to generate a pure transversal spin current density. The SOC effects that give rise to SHE in a nonmagnetic material may be due to the band structure of the material (intrinsic SHE) or by addition of high SOC impurities into the material (extrinsic SHE). As illustrated in figure 6, the spin polarization of the accumulated spins due to SHE is orthogonal to both the directions of the injected charge current as well as the spin current. Thus, the spin current generation using SHE can be described using the equation $J_s = \theta_{sh}(J_c \times \hat{\sigma})$, where $\hat{\sigma}$ is the spin polarization. Here, $\theta_{sh} (= J_s/J_c)$ is spin Hall angle of the nonmagnetic material and quantifies the efficiency of the spin current generation by SHE. For further details into SHE, the readers can refer to detailed reviews on SHE [51, 52].

For practical spintronic applications, it is desirable to have a higher spin Hall angle for efficient spin current generation using SHE. It is generally understood that the in-plane SOT efficiency in the ST-FMR technique estimates the spin Hall angle of the NM. Recently, many efforts have been devoted to obtain a large SOT efficiency and efficient SOT driven magnetization switching or precession via pure spin currents in HM/FM bilayers [2, 20-24]. Apart from ST-FMR measurements [25, 32], several different techniques have been also employed to determine the spin Hall angle, such as the lateral spin valve method [54-56], spin pumping [57] and spin Hall magnetoresistance (SMR) measurements [58]. In the following sub-sections, we first review the research progress of the SOT efficiency evaluation in HMs and alloys by the ST-FMR technique.

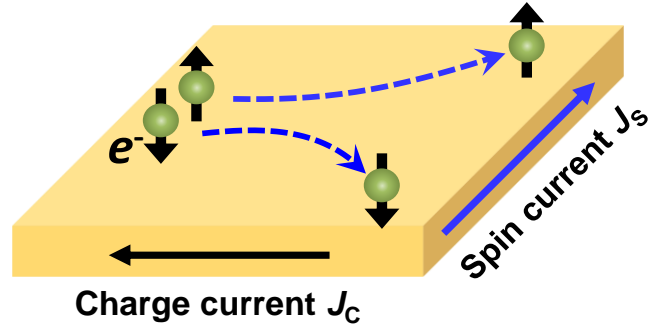


Figure 6. Schematic of SHE. The black-colored, blue-colored, and dotted arrows indicate the directions of charge current J_C , spin current J_S , and the motions of spin-up and spin-down electrons.

5.1. Spin Hall effect in Pt

Liu *et al.* first utilized ST-FMR to evaluate the SOT efficiency in the Pt (6 nm)/Py (4 nm) bilayer device at room temperature [25]. The schematic of a Pt/Py bilayer and the main results are shown in figure 7. The value of SOT efficiency in Pt is determined to be ~ 0.056 . Further, they have also utilized the MOD method as an independent check to confirm their results. By taking advantage of the large SOT efficiency, they also demonstrated the SOT driven magnetization switching in Pt/Co/Al₂O₃ trilayer structures [22].

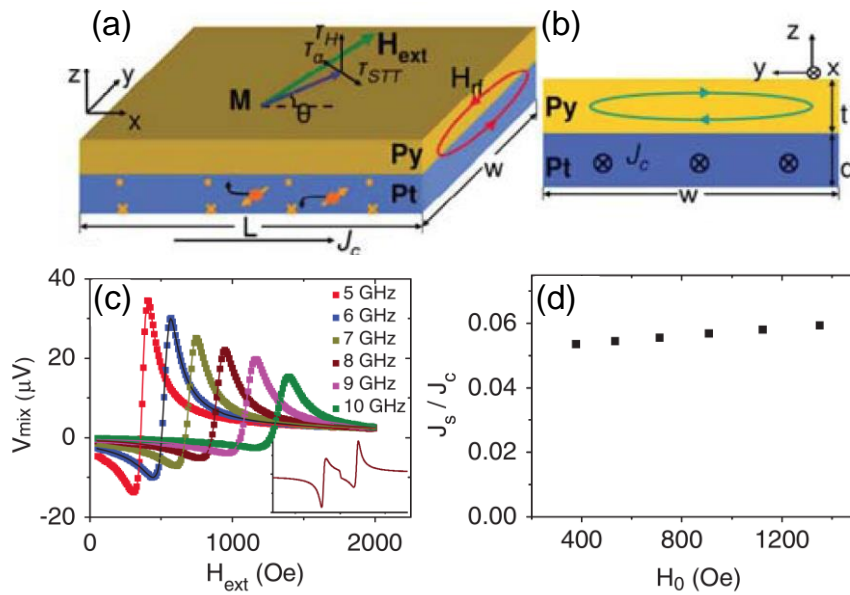


Figure 7. (a) Schematic of a Pt (6 nm)/Py (4 nm) bilayer illustrating the spin-orbit torque τ_{STT} , the Oersted field torque τ_{H} , and the direction of the damping torque τ_{α} . (b) Left-side view of the Pt/Py system, showing the Oersted field generated by the current flowing just in the Py layer, which should produce no net effect on the Py magnetization. (c) ST-FMR signals on a Pt/Py sample. The sample dimensions are 20 μm wide and 110 μm long. The inset shows the ST-FMR signal of 8 GHz in a full magnetic field range. (d) SOT efficiency in Pt/Py at different resonance fields. Reprinted with permission from [25]. Copyright (2011) by the American Physical Society.

Subsequently, the SOT efficiency in Pt has been quantified by different measurement methods in different research groups. However, there have been significant disagreements in the reported values of the SOT efficiency in Pt, ranging from ~ 0.012 to ~ 0.12 [32, 51, 52]. To figure out the possible reasons for this discrepancy and determine the intrinsic SOT efficiency value in Pt is of great importance. For ST-FMR measurements, the measured SOT efficiency is evaluated from the amount of spins that are absorbed by the FM layer. There are three aspects that affect the measured SOT efficiency. The first one is the spin diffusion in the Py layer since the spins can transmit into Py with a characteristic length (i.e. spin diffusion length), which is often ignored. Wang *et al.* [32] carried out Py thickness dependent ST-FMR measurements in Pt (6 nm)/Py ($t = 2 - 10$ nm) bilayers. It was found that θ_{sh} increases when the Py thickness increases as shown in figure 8(a). By taking into account the spin diffusion in the Py layer, the SOT efficiency of Pt is determined to be ~ 0.068 at room temperature [32]. The second aspect is spin diffusion in the Pt layer. J_{S} and the measured SOT efficiency θ_{sh} in a Pt film of thickness d should be reduced from the bulk value ($d = \infty$) by $J_{\text{S}}(d) = J_{\text{S}}(\infty) [1 - \text{sech}(d/\lambda_{\text{S}})]$ and $\theta_{\text{sh}} = \theta_{\infty} [1 - \text{sech}(d/\lambda_{\text{S}})]$, respectively [25, 32, 45, 59]. For example, the spin diffusion length, λ_{S} of Pt estimated from a Pt/Py device is ~ 1.5 nm [32] (figure 8(b)). The third aspect is the interface transparency as spin currents transmit through the Pt and Py interface, which is discussed in Section 5.4.

Figure 8(c) shows a summary of the SOT efficiencies as a function of λ_{S} in Pt measured by

different techniques from various research groups [25, 32, 58, 60-69]. A clear correlation between SOT efficiency θ_{sh} and λ_{S} is found, which is approximately an inverse relationship with $\theta_{\text{sh}}\lambda_{\text{S}} \sim 0.13 \text{ nm}$ (denoted by the blue thick line) [32]. The λ_{S} in a material is generally proportional to its electrical conductivity (σ) [32, 70]. Figure 8(d) shows an approximately linear relationship between the reported λ_{S} and σ in Pt films [32, 45, 55, 58-62, 64, 67, 71]. Therefore, the SOT efficiency is inversely related to the conductivity of the HMs. All the data in figures 8(c) and (d) were measured at room temperature, except for those from Refs. [61] and [71] which were measured at 10 K, as denoted by small black stars. In addition, it was found that the θ_{sh} in Pt remains almost constant as temperature decreases from 300 to 13 K [32, 55].

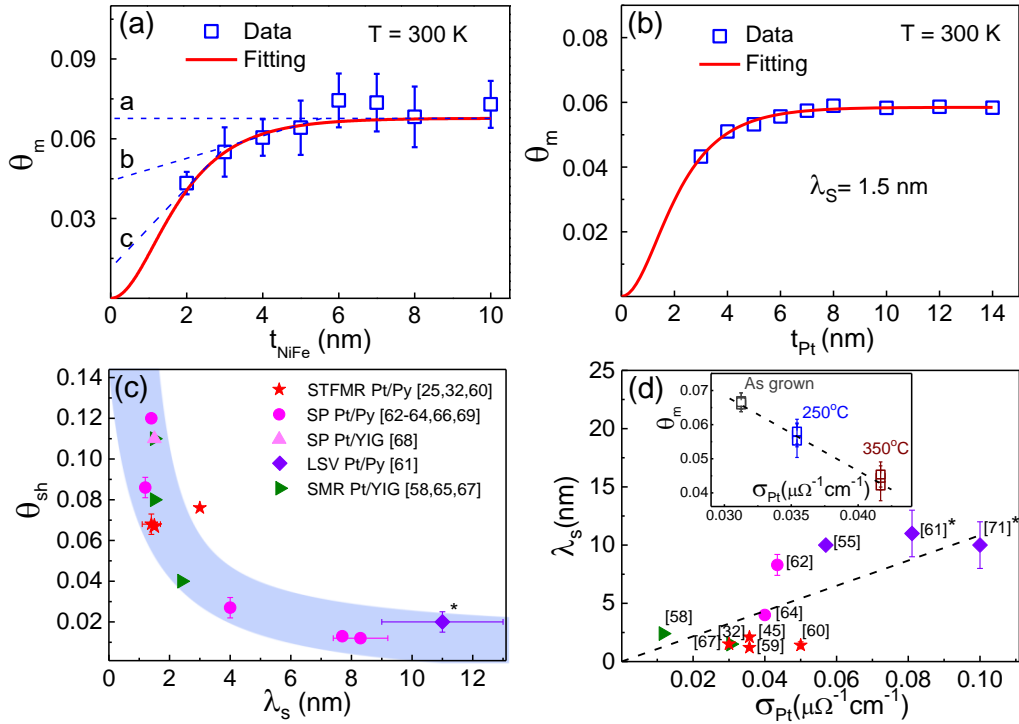


Figure 8. (a) Measured SOT efficiency θ_{sh} for Pt/Py(t) devices with different Py thicknesses from ST-FMR measurements at 8 GHz and 300 K. (b) θ_{sh} (blue squares) of Pt(4 nm)/Py(4 nm) devices as a function of Pt thickness at 300 K. (c) Summarized SOT efficiency θ_{sh} as a function of λ_{S} in Pt from various reports. The ST-FMR, SP, LSV, and SMR represent spin torque ferromagnetic resonance, spin pumping, nonlocal measurement in lateral spin valves, and spin Hall

magnetoresistance method, respectively. The blue thick curve shows a correlation $\theta_{\text{sh}}\lambda_{\text{S}} \sim 0.13$ nm. (d) λ_{S} in Pt as a function of its electrical conductivity (σ_{Pt}). The inset shows the measured SOT efficiency in various Pt films with different conductivities. The dashed lines serve as guide for the eye. Adapted from [32], with the permission of AIP Publishing.

It is possible that in ST-FMR measurements, spin pumping can also occur due to the inverse spin Hall effect by $J_{\text{C}} = \theta_{\text{sh}}(J_{\text{S}} \times \hat{\sigma})$. Therefore, an additional dc voltage (V_{SP}) can also be produced and might contaminate the ST-FMR signals. The spin pumping contributions for Pt (6 nm)/Py ($t = 2 - 10$ nm) bilayers have been estimated in Ref. [32], by using the following equations in the method part in Ref. [40].

$$V_{\text{SP}} = \theta_{\text{sh}} \frac{eW\lambda_{\text{S}}R}{2\pi} \tanh\left(\frac{d}{2\lambda_{\text{S}}}\right) \text{Re}(g_{\uparrow\downarrow}^{\text{eff}}) \omega(\theta_{\text{c}})^2 \sin(\theta_{\text{H}}) \sqrt{H_0/(H_0 + 4\pi M_{\text{eff}})},$$

$$\theta_{\text{c}} = \frac{1}{dR/d\theta_{\text{H}}} \frac{2}{I_{\text{RF}}} \sqrt{(V_{\text{S}})^2 + (V_{\text{A}})^2},$$

where W is the channel width, R is the device resistance, d is the Pt thickness, $\text{Re}(g_{\uparrow\downarrow}^{\text{eff}})$ is the real part of the effective spin mixing conductance ($\approx 2 \times 10^{19} \text{ m}^{-2}$), θ_{c} is the maximum precession cone angle in the device plane, and V_{S} and V_{A} are the symmetric and antisymmetric components of the ST-FMR signal, respectively. It was found that the estimated spin pumping signals V_{sp} are at least one order of magnitude smaller than the ST-FMR symmetric component V_{S} . It is known that V_{sp} is proportional to device resistance [57]. Since the resistance of the ST-FMR device is usually small ($\sim 50 \Omega$ for the impedance matching, the spin pumping contributions in the ST-FMR measurements are usually much smaller than the ST-FMR signals.

In addition, the SOT efficiency in Pt/Py bilayers has been quantified by the $V_{\text{S}}/V_{\text{A}}$ ratio and only- V_{S} methods separately [32], and no clear difference between the SOT efficiencies from these two methods was found. This suggests that there is negligible τ_{FL} arising from the Pt/Py interface.

However, it has been also reported that τ_{FL} might arise from the Rashba effect at the Pt/FM interface [20, 38, 72], which indicates that the characteristics of the interfaces, such as the interface quality and the degree of oxidation of the interfaces, could also affect the SOT efficiency. On the other hand, a Cu with negligible SOC or other insertion layers can be inserted between the HM and FM layer to eliminate or modify the interface SOT effect [46, 73, 74].

5.2. Spin Hall effect in Ta

In 2012, a large SOT efficiency and giant spin Hall induced magnetization switching were reported in a Ta (8 nm)/Co₄₀Fe₄₀B₂₀ (CoFeB, 4 nm) bilayer at room temperature [21]. Figures 9(a) and (b) illustrate the ST-FMR measurements and results in a Ta/CoFeB bilayer. A very high SOT efficiency of ~ 0.15 was determined by the V_s/V_A ratio method. The SOT efficiency shows a negative sign compared to the positive sign in Pt, which agrees with the opposite character of spin accumulation in Pt and Ta. Moreover, an efficient SOT driven magnetization switching was first realized in a three terminal MTJ device (Ta/CoFeB/MgO/CoFeB), which opens a new avenue to the SOT based spintronic devices.

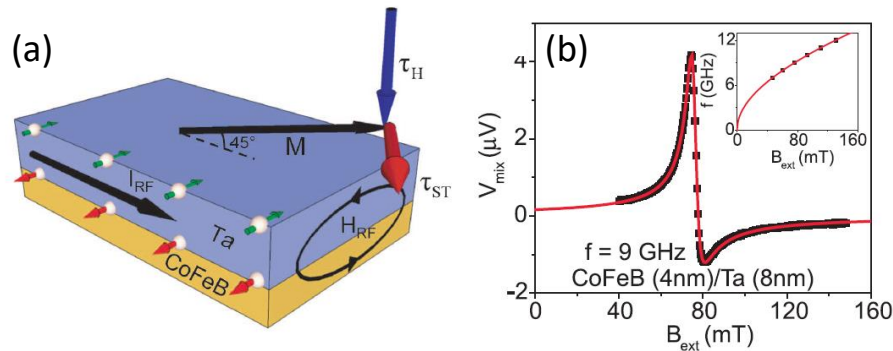


Figure 9. (a) Schematic of sample geometry for a Ta (8 nm)/CoFeB (4 nm) bilayer ST-FMR device. (b) ST-FMR signal at $f = 9$ GHz. From [21]. Reprinted with permission from AAAS.

The interface effect between the Ta and CoFeB layer has not been considered by Liu *et al.* [21] in the Ta SOT efficiency evaluation. Thus, we compare the SOT efficiency in Ta on Si/SiO₂

substrate/Co₄₀Fe₄₀B₂₀ (4 nm)/Ta (8 nm) and Si/SiO₂ substrate/Py (4 nm)/Ta (8 nm) devices by ST-FMR measurements at different temperatures. A significant contribution of field-like torque, τ_{FL} , is observed, which might arise from the interface between Ta and CoFeB layers. Figure 10(a) shows ST-FMR signals and fits (solid lines) in a CoFeB (4 nm)/Ta (8 nm) device for frequencies between 6–10 GHz at room temperature. The H_{ext} is swept at an angle of $\theta_{\text{H}} = 35^\circ$ with respect to the I_{RF} . The SOT efficiency in Ta is quantified by the $V_{\text{S}}/V_{\text{A}}$ ratio and only- V_{S} methods, respectively. As shown in figure 10(b), the in-plane SOT efficiency (θ_{sh}) in CoFeB/Ta device is ~ 0.109 from the $V_{\text{S}}/V_{\text{A}}$ ratio method at room temperature and it remains in the range of ~ 0.1 – 0.15 at most of temperatures. The θ_{sh} value is similar to the previous report [21]. In addition, we perform the only- V_{S} method to determine θ_{sh} as well as the out-of-plane SOT efficiency (θ_{\perp}) which characterizes the τ_{FL} . Surprisingly, the θ_{sh} value from the only- V_{S} method is ~ 0.02 at room temperature as shown by the red circles in figure 10(b). This big inconsistency in θ_{sh} indicates a significant τ_{FL} (i.e. θ_{\perp}) contribution in the CoFeB/Ta bilayer. As shown in figure 10(c), there is indeed a large θ_{\perp} of ~ 0.044 in a CoFeB/Ta bilayer at room temperature. This result is qualitatively similar to an earlier report of a larger τ_{FL} in CoFeB/Ta compared to τ_{DL} [75].

Similarly, we also characterize the Py (4 nm)/Ta (8 nm) bilayer device. As shown in figure 10(d), the θ_{sh} from the only- V_{S} method is ~ 0.01 at room temperature. The small inconsistency in θ_{sh} from two analysis methods indicates that the τ_{FL} is not significant in the Py/Ta bilayer. Finally, θ_{sh} in Ta is ~ 0.01 – 0.02 obtained from the FM/Ta bilayer using ST-FMR at room temperature, which is consistent with other reports [61, 76-78]. The slightly different θ_{sh} from Py/Ta and CoFeB/Ta can be attributed to the different interface transparency [76, 79-81]. The θ_{sh} (from only- V_{S}) almost remains constant from 15 to 300 K, while the θ_{\perp} shows a fast decrease at low temperature range, suggesting that θ_{sh} and θ_{\perp} might come from different origins. Moreover, we observed a similar θ_{sh}

of ~ 0.01 – 0.015 in Py (20 nm)/Ta (6–25 nm) and CoFeB (15 nm)/Ta (15 nm) bilayers by spin pumping measurements at room temperature. This similar SOT efficiencies from both ST-FMR and spin pumping measurements suggest the Onsager reciprocity, which has been also demonstrated recently [82].

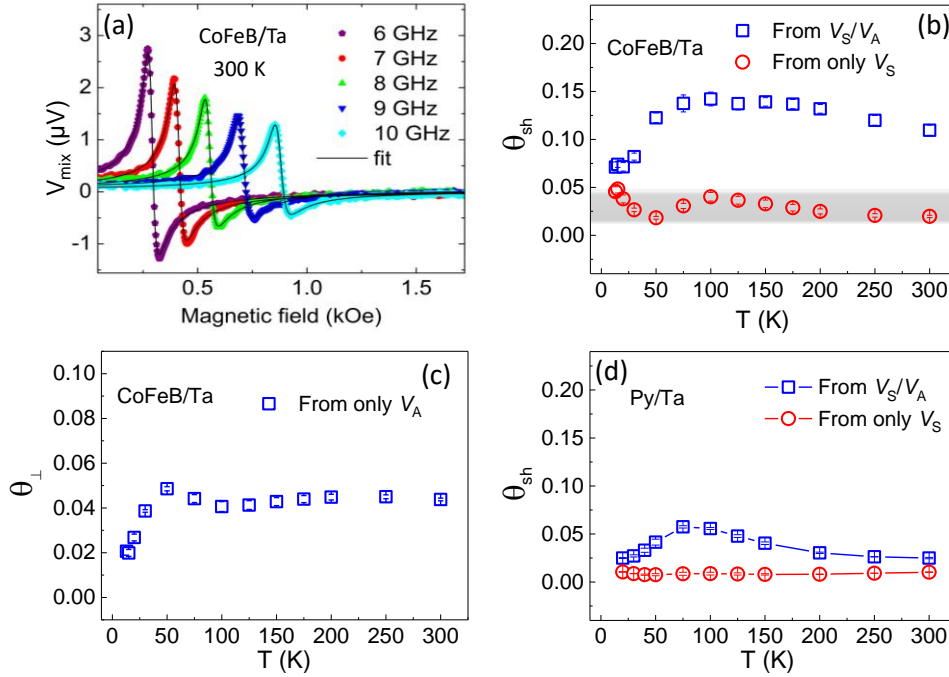


Figure 10. (a) ST-FMR measurements in a CoFeB (4 nm)/Ta (8 nm) device at different frequencies. The symbols are the measured data, and the solid lines are fits by sum of Lorentzian functions. (b) The in-plane SOT efficiency and (c) the out-of-plane SOT efficiency in Ta as a function of temperature obtained from ST-FMR measurements on the CoFeB (4 nm)/Ta (8 nm) device. (d) The in-plane SOT efficiency as a function of temperature in the Py (4 nm)/Ta (8 nm) device.

Figure 11 shows a summary of the SOT efficiencies in Ta films, ranging from 0.0037 to 0.26, measured by different techniques from different research groups [61, 75-77, 83-89]. The fit of θ_{sh} as a function of λ_S indicates an approximately inverse relationship with $\theta_{sh}\lambda_S \sim 0.036$ nm (denoted by the blue thick line). However, it is observed that the correlation between θ_{sh} and λ_S is not as clear as the case of Pt as shown in figure 8(c), which might be due to multi-phases (such as α -, β -

phases or amorphous film) in different Ta thin films [21, 87].

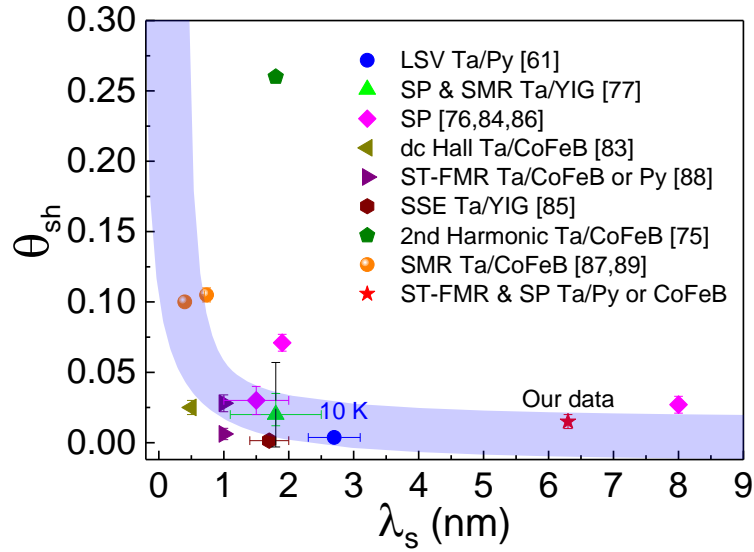


Figure 11. Summarized SOT efficiency θ_{sh} as a function of λ_s in Ta from various reports. The LSV, SP, SMR, dc Hall, ST-FMR, SSE represent nonlocal measurement in lateral spin valves, spin pumping, spin Hall magnetoresistance, Hall measurements by using dc currents, spin torque ferromagnetic resonance, and spin seebeck effect method, respectively. The blue thick curve shows a correlation of $\theta_{sh}\lambda_s \sim 0.036$ nm. The θ_{sh} and λ_s were obtained at room temperature, except for the one by the LSV method which was measured at 10 K as denoted in the figure.

5.3. Spin Hall effect in tungsten (W) and other alloys with heavy metal dopants

For the case of pure HMs, the largest SOT efficiency is ~ 0.3 observed in a β -phase W/CoFeB bilayer by ST-FMR measurements at room temperature [35]. This value is about two times larger than that in Ta, leading to efficient spintronic devices. Taking advantage of the highly efficient spin current generation, SOT driven magnetization switching has been demonstrated in a β -phase W based 3-terminal MTJ device [35]. The critical switching current density, J_C , is in the order of $\sim 10^6$ A/cm² in W/CoFeB/MgO [90], which is almost one order of magnitude smaller than that in Pt.

Figure 12 shows a summary of the SOT efficiencies in W, ranging from 0.0043 to 0.95, measured by different techniques from different research groups [84, 85, 87, 89-93]. However, the

correlation between θ_{sh} and λ_s is not as clear as the case of Pt as shown in figure 8(c). Similar to the case of Ta, the reason can be attributed to the multi-phases (such as α -, β -phases) in various W thin films [35, 90].

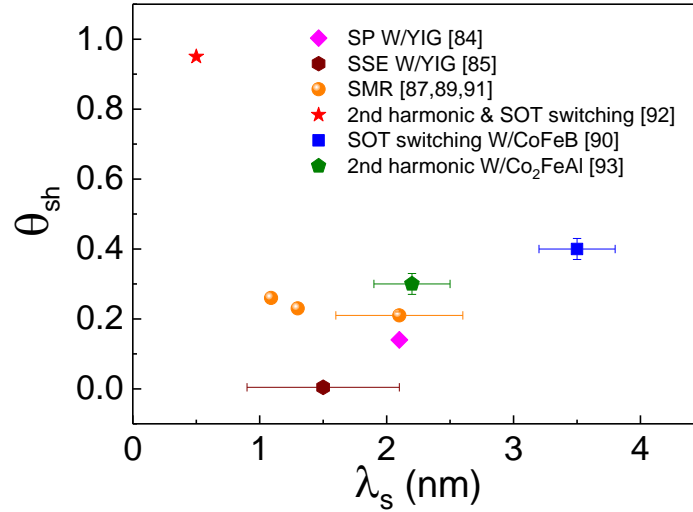


Figure 12. Summary of SOT efficiency θ_{sh} as a function of λ_s in W from various reports. The SOT switching represents current induced magnetization switching via SOT. All data were obtained at room temperature.

Besides the pure HMs, alloys consisting of a light metal with heavy metal dopants have been also investigated [94-97]. Ramaswamy *et al.* [97] experimentally studied the effects on the SOT efficiency due to a systematic addition of Pt into the light metal Cu by ST-FMR measurements. As shown in figures 13(a) and (b), the SOT efficiency of $Cu_{1-x}Pt_x$ increases as the Pt concentration increases from 0 to 40%. It was found that only 28% Pt in $Cu_{1-x}Pt_x$ can give rise to a SOT efficiency close to that of Pt. Since Cu is the most common metallization element in the CMOS platform and $Cu_{1-x}Pt_x$ can have a large enough SOT efficiency, the $Cu_{1-x}Pt_x$ -based alloy is easier to integrate the spintronic devices into an existing Si fabrication technology. In addition, from further analysis of the ST-FMR data, it is found that the skew scattering contribution is significant for lower Pt concentrations, while the side-jump contribution is significant for higher Pt concentrations. This

result can be understood as due to the different scaling of the contributions of skew scattering and side-jump with respect to Pt concentrations. As Pt concentration increases, the longitudinal resistivity increases. In a simplistic picture, the skew-scattering contribution is independent of this increased resistivity due to Pt, whereas the side-jump contribution is proportional to this increased resistivity [98, 99]. Thus, for higher Pt concentrations, the increase in the resistivity is larger, leading to the domination of the side-jump contribution. Furthermore, this result can be also correlated with an earlier theoretical report [100] and with experiments in the context of anomalous Hall effect due to rare earth impurities in Gd [101].

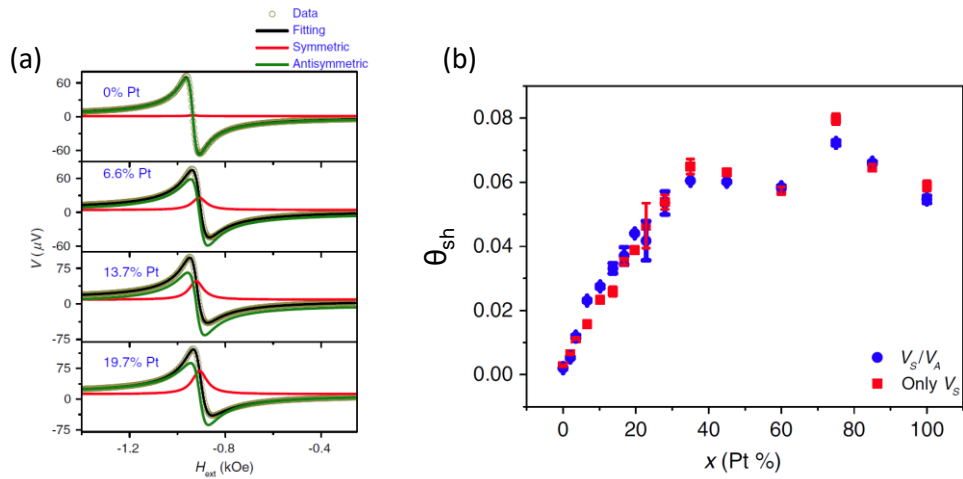


Figure 13. Fittings of ST-FMR signals from the $\text{Cu}_{1-x}\text{Pt}_x$ (6 nm)/Py (5 nm) bilayer for $x = 0, 6.6, 13.7,$ and 19.7% in the negative H_{ext} range for an applied microwave power of 16 dBm and a microwave frequency of 8 GHz. As the Pt concentration increases, the amplitude of the symmetric component increases (red curve). (b) SOT efficiency, θ_{sh} , for different Pt concentrations extracted from ST-FMR fittings by using the V_S/V_A ratio method (blue circles) and only- V_S method (red squares), suggesting there is a negligible τ_{FL} at the interface between $\text{Cu}_{1-x}\text{Pt}_x$ and Py. Reprinted with permission from [97]. Copyright (2017) by the American Physical Society.

5.4. Role of interface transparency of HM and FM in the SOT efficiency

It is possible for the spin loss to occur at the interfaces when the spins transmit into the FM layer from the spin generation sources [70, 79], which can have an important role in the estimated

SOT efficiency. Using the ST-FMR technique, Zhang *et al.* [80] studied the transparency of Pt (6 nm)/Py (5.5 nm) and Pt (6 nm)/Co (5.2 nm), shown in figures 14(a) and (b), respectively. Using standard ST-FMR analysis method, the authors find that the SOT efficiency in Pt/Co is ~ 0.11 , much larger than ~ 0.05 in Pt/Py. They ascribed the discrepancy of the SOT efficiency to the interface transparency, which is correlated to the effective spin-mixing conductance, G_{eff} at the Pt and FM interface. They quantified the G_{eff} to be $3.96 \times 10^{19} \text{ m}^{-2}$ (for Pt/Co) and $1.52 \times 10^{19} \text{ m}^{-2}$ (for Pt/Py), and the interface transparencies to the spin currents are ~ 0.65 (Pt/Co) and ~ 0.25 (Pt/Py), respectively. After taking into account the transparencies of these interfaces, they found that the intrinsic SOT efficiency in Pt has a much higher value of 0.17 ± 0.02 in Pt/Co and 0.20 ± 0.03 in Pt/Py bilayer. Further, this result also suggests that the spins easily transmit through the Pt/Co interface and thus give a large measured SOT efficiency, which might be due to better matching of the electronic bands between the Pt and Co layer compared to the Pt and Py layer.

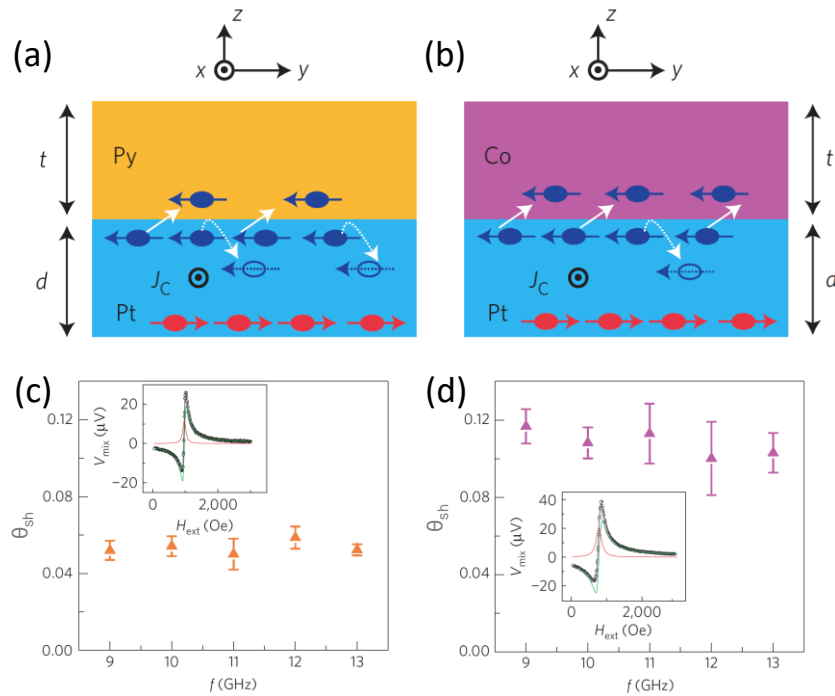


Figure 14. Illustration of the interface transparency for (a) Pt/Py and (b) Pt/Co: the red and blue arrows represent the up and down spin accumulation. The white arrows show the electrons diffusing across or being reflected at the interface. Frequency dependence of measured SOT efficiencies for (c) Pt (6 nm)/Py (5.5 nm) and (d) Pt (6 nm)/Co (5.2 nm). Insets: measured ST-FMR signals for Pt/Py and Pt/Co at 9 GHz, respectively. Reprinted by permission from Macmillan Publishers Ltd: Nature Physics [80], copyright 2015.

Subsequently, Pai *et al.* [81] also conducted a systematic study of the interface transparency in Pt/Co and Pt/CoFe bilayers. They found that the SOT efficiency can be modulated under different interface conditions and a much larger intrinsic SOT efficiency (~ 0.3) in Pt is obtained after considering the interface transparency between the Pt and FM layer. This value is much larger than the measured value of ~ 0.06 [25, 32], suggesting that there is a large spin memory loss at the interface. Therefore, it is understood that the measured SOT efficiency by ST-FMR technique represents a lower value because of the interface transparency. Therefore, modification or enhancement of the SOT efficiency via interface transparency engineering, such as inserting layers between the HM and FM [73, 74], manipulation of the film crystal structures [102] or using different combinations of HM and FM layers [80, 81], are some interesting and important on-going research activities.

5.5. Difference in the SOT efficiency between ST-FMR and magnetization switching technique

From ST-FMR measurements, τ_{DL} and τ_{FL} can be separately extracted due to the 90° phase difference in the magnetization dynamics (see Section 2.3) [33, 40]. Subsequently, τ_{DL} can be used to evaluate the in-plane SOT efficiency θ_{sh} . However, for the case of current driven magnetization switching using SOT, it has been reported that both τ_{DL} and τ_{FL} contribute to the magnetization switching and the switching current density J_C might be significantly reduced if there is an additional τ_{FL} [103-106], which can lower the energy barrier of magnetization switching. Therefore,

the values of the SOT efficiency derived from SOT induced magnetization switching measurements can be greater than that from ST-FMR measurements. In addition, during the ST-FMR measurements, the magnetization is uniformly aligned in the direction of an applied large external magnetic field. Hence, it is a coherent magnetization precession process. However, the current induced magnetization switching proceeds through an thermally excited incoherent magnetization switching process [107, 108] (i.e. domain wall motion with a much lower energy barrier), which can also lead to a smaller J_C and a larger θ_{sh} from magnetization switching measurements compared to the ST-FMR measurements. Therefore, these aspects should be taken into account for the SOT efficiency evaluation or comparison between ST-FMR and switching measurements.

6. SOT in topological insulators (TIs)

Topological insulators (TIs) are quantum materials that have a band gap just like a normal insulator but have topologically protected conducting edge states or surface states resulting from the inverted conduction and valence bands due to strong SOC [109-112]. TI materials started from two-dimensional (2D) system, called 2D TI. The 2D TI was predicted [113] and experimentally observed in HgTe/CdTe quantum wells structures in 2007 [109]. As shown in figure 15(a), two conductive edge states are present in the edge of 2D TIs, each of which contributes one quantum of conductance e^2/h , where h is the Plank's constant. In the edge states, the spin polarization depends on the electron momentum.

A year later, in 2008, the first 3D topological insulator $\text{Bi}_{1-x}\text{Sb}_x$ was experimentally discovered [114]. Since then, more 3D TIs such as Bi_2Se_3 , Bi_2Te_3 , and Sb_2Te_3 , having a larger bandgap and single Dirac cone at the Γ point, have been predicted and identified mainly by angle resolved photoemission spectroscopy (ARPES) experiments [110-112]. The 3D TIs possess spin-

momentum-locked topological surface states (TSS) due to time reversal symmetry protection [115-117] and it can be described by the Dirac Hamiltonian $H_k = v_F (\hat{z} \times \hat{\sigma}) \cdot k$, where k is electron momentum, \hat{z} is the unit vector perpendicular to the TI films and v_F is the Fermi velocity. This dispersion relationship reveals that on the TSS, the electron momentum and the spin polarization directions are strongly locked as shown in figure 15(b). As depicted in figure 15(c), in real space, as charge currents flow on TSS, all the electron spins are expected to be fully polarized in the orthogonal direction to the electron moving direction due to the topologically protection [118]. Therefore, a very efficient spin current generation and thus a giant SOT efficiency are expected in TIs due to TSS. For further details into TIs and related physics phenomena, the readers can refer to detailed reviews on TIs [116, 117]. In the following part, we will review research works on 3D TIs in the context of SOT efficiency determination.

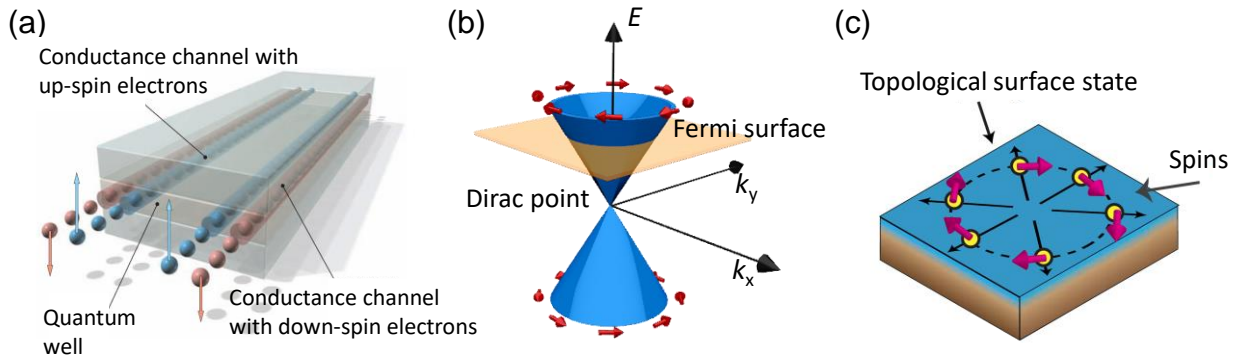


Figure 15. (a) Schematic of the spin momentum locked edge states in a quantum spin Hall insulator (i.e. 2D TI). From [109]. Adapted with permission from AAAS. (b) Schematic of Dirac cone of the TSS, illustrating the Dirac point (DP), Fermi level (E_F) and spin momentum locking in momentum space. Reprinted with permission from [33]. Copyright (2015) by the American Physical Society. (c) Illustration of the electron flow and spin polarizations on the surface of TI for opposite applied charge currents. Adapted with permission from [118]. Copyright (2014) by the American Physical Society.

6.1. SOT efficiency in TIs

Research works have been conducted to demonstrate the TSS and quantify the SOT efficiency in TI/FM heterostructures [33, 34, 40, 118-126]. In 2014, Mellnik *et al.* [40] studied the Bi₂Se₃ (8 nm)/Py (16 nm) bilayers by ST-FMR measurements at room temperature. Figures 16(a) and (b) show the schematic of the bilayer structure and the representative ST-FMR signal. Using the only- V_S analysis method, the in-plane SOT efficiency, θ_{sh} , was determined to be ~ 2.0 – 3.5 at room temperature, which is about one to two orders of magnitude larger than that in HMs reported previously. In addition, the out-of-plane SOT efficiency, θ_{\perp} , arising from τ_{FL} has the similar order of amplitude as θ_{sh} . The spin configuration is consistent with that expected in the TSS of TIs [115-117]. However, the exact mechanisms for this large SOT efficiency observed in Bi₂Se₃ was not clear at that time.

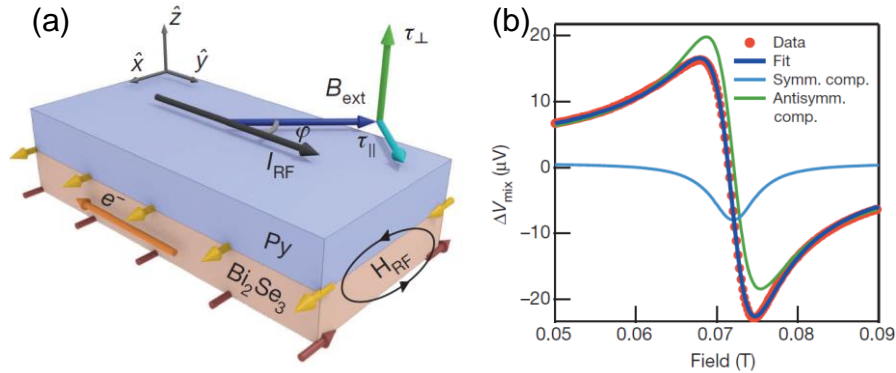


Figure 16. (a) Schematic diagram of Bi₂Se₃ (8 nm)/Py (16 nm) bilayer structure. The yellow and red arrows denote spin moment directions. (b) Measured ST-FMR signal at room temperature with $f = 8$ GHz and $\varphi = 45^\circ$. A fixed microwave power of 5 dBm is absorbed by the device, corresponding to $I_{RF} = 7.7 \pm 1.1$ mA. The lines are the fits showing the symmetric and antisymmetric components. Reprinted by permission from Macmillan Publishers Ltd: Nature [40], copyright 2014.

Subsequently, Wang *et al.* [33] verified that the observed SOTs originate from the TSS in Bi₂Se₃ by temperature-dependent ST-FMR measurements on a Bi₂Se₃ (20 nm)/CoFeB (5 nm)

heterostructure. By taking the only- V_S and $-V_A$ analysis method, the authors determined both θ_{sh} and θ_{\perp} as a function of temperature from three representative ST-FMR devices. As shown in figure 17(a), the θ_{sh} was found to increase steeply and nonlinearly, especially below 50 K, reaching the value of ~ 0.42 , which is almost 10 times larger than that at 300 K. Moreover, a difference in the θ_{sh} values between two ST-FMR analysis methods indicates a noticeable τ_{FL} (i.e. θ_{\perp}), which is plotted against temperature in figure 17(b). As it is known that the θ_{sh} arising from the bulk spin Hall mechanism normally shows a very weak temperature dependence [32, 55, 96], and the θ_{\perp} arising from the field-like torque or interfacial Rashba effect usually shows a smaller value at low temperature in HMs or semiconductors [75, 127, 128]. In addition, the hexagonal warping effect in the TSS can account for the out-of-plane spin polarizations and thus affect the θ_{\perp} [129-132]. Therefore, the significant increase of θ_{sh} and θ_{\perp} in the $\text{Bi}_2\text{Se}_3/\text{CoFeB}$ bilayer as temperature decreases is attributed to the TSS in Bi_2Se_3 . These results suggest that the TSS with spin momentum locking can play an important role in the spin current generation. This work suggests that the bulk states (BS) in Bi_2Se_3 and the 2DEG on top of Bi_2Se_3 can lead to a contamination to the SOT effects from TSS. In Section 6.3, we present the role of BS, 2DEG and TSS of Bi_2Se_3 in the SOT efficiency by ST-FMR measurements.

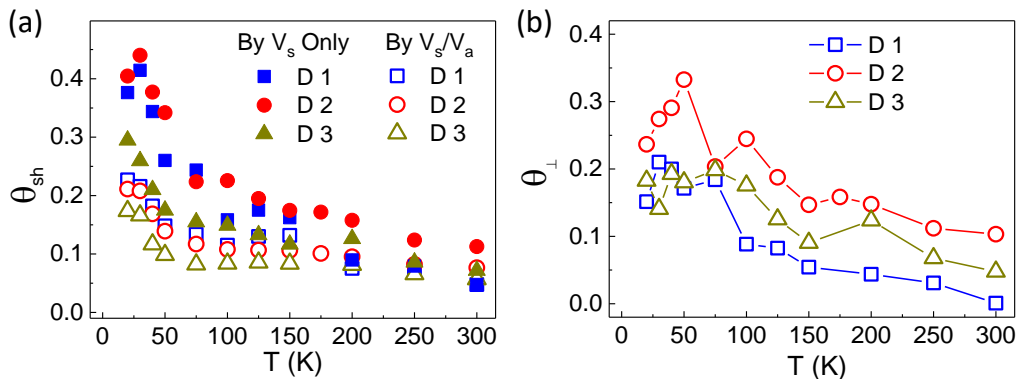


Figure 17. Temperature dependence of (a) in-plane SOT efficiency, θ_{sh} , and (b) out-of-plane SOT efficiency, θ_{\perp} , in Bi_2Se_3 (20 nm)/CoFeB (5 nm) for three devices: D1, D2, and D3. The SOT

efficiencies are analyzed by two different methods: by only- V_S and by V_S/V_A ratio. Reprinted with permission from [33]. Copyright (2015) by the American Physical Society.

The Fermi level dependent SOT efficiency was recently studied in a $(\text{Bi}_{1-x}\text{Sb}_x)_2\text{Te}_3$ (BST, 8 nm)/Cu (8 nm)/Py (10 nm) [120]. As shown in figure 18(a), the Fermi level position relative to the Dirac point was controlled by using different Sb compositions. From ST-FMR measurements on each device, it was observed that the *interface* charge-to-spin conversion efficiency, q_{ICS} due to the TSS exhibits a large and nearly constant value for $0 < x < 0.7$ (see figure 18(b)), suggesting the highly efficient charge and spin interconversion in the TSS of TI materials. However, the q_{ICS} was found remarkably reduced as the Fermi level traverses through the Dirac point, which is possibly due to the inhomogeneity of k_F and/or instability of the helical spin structure near the Dirac point.

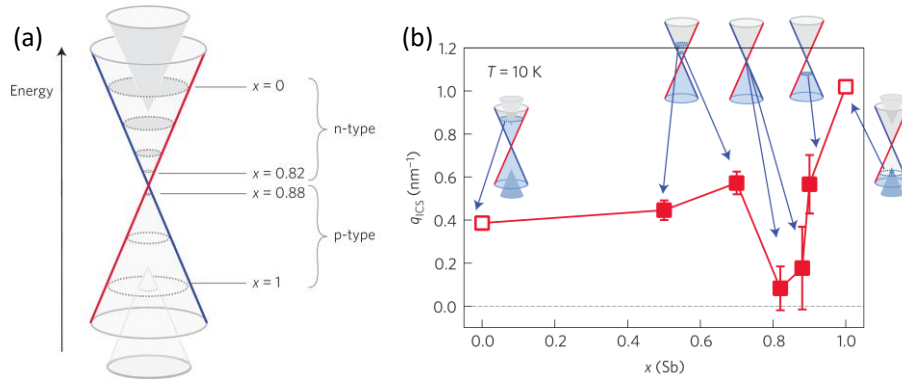


Figure 18. (a) Schematic of the energy dispersion and Fermi level position in $(\text{Bi}_{1-x}\text{Sb}_x)_2\text{Te}_3$ with different Sb composition. (b) Interface charge-to-spin conversion efficiency, q_{ICS} as a function of Sb composition. The inset shows the band structure and Fermi level position for each Sb composition. Bulk insulating BST with $0.50 \leq x \leq 0.90$ should have only surface transport. Bi_2Te_3 ($x = 0$) and Bi_2Sb_3 ($x = 1$) have both bulk and surface conduction paths. Reprinted by permission from Macmillan Publishers Ltd: Nature Physics [120], copyright 2016.

6.2. Anisotropic SOT (efficiency) in Bi_2Se_3 MBE films

Bi_2Se_3 has a three-fold symmetry when viewed from the top (along the z -axis) shown in figures 19(a) and (b). Therefore, the molecular beam epitaxy (MBE) grown Bi_2Se_3 films naturally have

triangular islands as captured by atomic force microscope in figure 19(c). It is found that the orientation of the triangular islands prefers to a certain axis with twin structures due to the six-fold symmetric sapphire substrate. Although the anisotropy of electron transport has been observed in Bi₂Se₃ films previously [133], the anisotropy of SOT in Bi₂Se₃ has not been reported.

We have performed ST-FMR to study the anisotropic SOT characteristics in high quality MBE grown Bi₂Se₃ films shown in figure 19(c). Bi₂Se₃ Hall bars with different angle φ , the angle between the channel current (I) direction with respect to the x -axis denoted in figure 19(c), were fabricated in the same sample. Similarly, using the same Bi₂Se₃ wafer, ST-FMR devices of Bi₂Se₃ (10 QL)/CoFeB (7 nm) devices with different angle φ were also fabricated for the ST-FMR measurements. As shown in figures 19(d-e), both the resistivity ($\rho_{\text{Bi}_2\text{Se}_3}$) and sheet carrier concentration (n_{2D}) show angular dependent behaviors with the oscillation period of 60°. Furthermore, the in-plane SOT efficiency, θ_{sh} , in figure 19(f) also shows an oscillation behavior as the current I flows along different crystal axes (i.e. different angle φ). The oscillation period is also 60°, in which θ_{sh} has a low value at $\varphi = 0^\circ$ but a high value at $\varphi = 30^\circ$, and returns to a low value at $\varphi = 60^\circ$. This is consistent with the six-fold symmetry by considering the Bi₂Se₃ twin structures. Thus, this oscillation of the SOT efficiency is attributed to the hexagonal warping in the Fermi surface of the Bi₂Se₃ films [129, 132, 134]. An out-of-plane spin polarization in the TSS has been experimentally observed in Bi₂Se₃ [130, 131] due to the hexagonal warping effect, which shows a finite amplitude along the Γ -K direction but almost zero along the Γ -M direction in momentum space, leading to an oscillation period of 60° in the out-of-plane spin polarization. If we assume that the total spin polarization is unity in TSS, the in-plane spin polarization should also show the same oscillation period of 60°, which is in line with our observation.

Note that since the width of the current channel of the Hall bars and ST-FMR devices is 20

μm , which is much larger than the triangle size of $\sim 100\text{--}200\text{ nm}$ in figure 19(c), our data only show the averaged transport results. In addition, there exists nonuniform Bi_2Se_3 microstructures and devices with different φ are located different places on a sample. Consequently, a fluctuation of the high (or low) values at each angle φ can be observed in figures 19(d-f). Note that the similar anisotropy behavior is expected in the range of $\varphi = 180 - 360^\circ$ due to the crystal symmetry. Rather than rotating the crystal direction in different devices, the angular dependent ST-FMR measurements in one device can be combined to characterize the anisotropy of SOTs [135], which will be discussed in Section 7.2. Therefore, the ST-FMR is a suitable dynamic measurement method to study the anisotropy of SOTs.

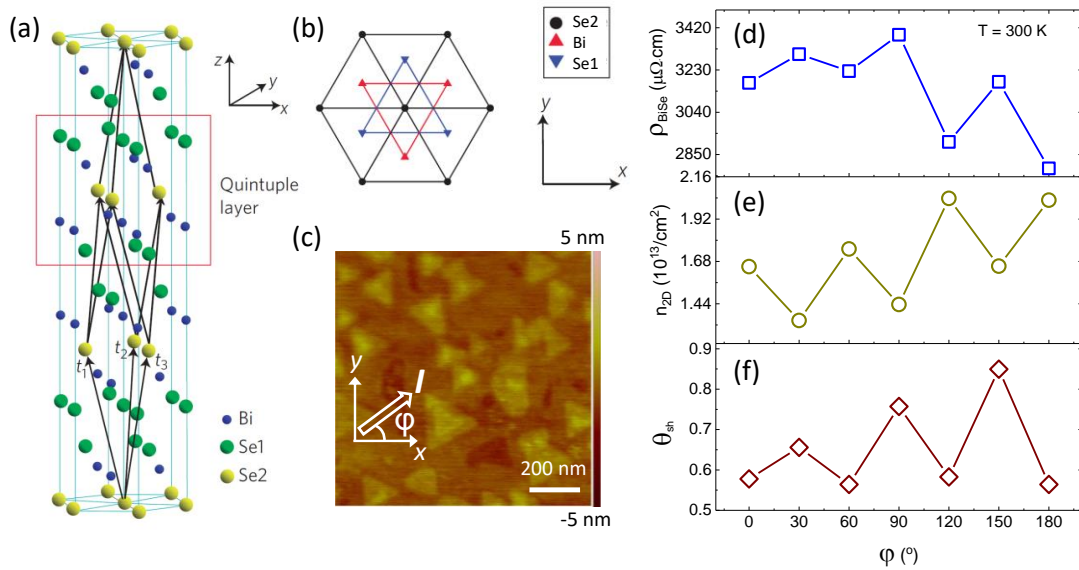


Figure 19. (a) Crystal structure of Bi_2Se_3 with three primitive lattice vectors denoted as $t_{1;2;3}$. A quintuple layer (1 QL $\approx 1\text{ nm}$) with Se1–Bi1–Se2–Bi1’–Se1’ is indicated by the red square. Adapted by permission from Macmillan Publishers Ltd: Nature Physics [111], copyright 2009. (b) Top view along the z -direction. The triangle lattice in 1 QL has three different positions, denoted as Se2, Bi and Se1. Adapted by permission from Macmillan Publishers Ltd: Nature Physics [111], copyright 2009. (c) Atomic force microscope image of a 10-QL Bi_2Se_3 film with a roughness of $\sim 0.5\text{ nm}$. Triangular islands are observed with a clear terrace step of 1 QL, indicating a high quality Bi_2Se_3 film. (d-f) The Bi_2Se_3 resistivity, sheet carrier concentration and in-plane SOT efficiency

measured with charge currents flowing along different crystalline directions. The angle φ is denoted in (c).

6.3. TSS dominated SOT

As mentioned earlier, the BS, 2DEG, and TSS usually coexist in TIs such as Bi_2Se_3 . Therefore, it is important to understand the role of each channel on the SOT efficiency in TIs, so that one can maximize the SOT efficiency to realize highly efficient SOT driven magnetization switching. Figure 20 shows a summary of the reported SOT efficiencies in various TIs with different thicknesses. The SOT efficiency increases significantly as TI films become thinner even though SOT efficiencies are evaluated using different techniques and in different TIs. Recently, the SOT efficiency of MBE grown Bi_2Se_3 films with various thicknesses in the range of 5 to 20 QL has been quantified by ST-FMR measurements [34]. The optimum thickness range of Bi_2Se_3 has been identified to be 5–8 QL to maximize the SOT effect in Bi_2Se_3 devices. Figure 21(a) shows the schematic of the film stack used for the ST-FMR measurements. First, it was found that the resistivity, $\rho_{\text{Bi}_2\text{Se}_3}$ rapidly increases when the Bi_2Se_3 thickness ($t_{\text{Bi}_2\text{Se}_3}$) is less than 10 QL as shown in figure 21(b). On the other hand, the sheet carrier concentration ($n_{2\text{D}}$) shows an opposite trend, decreasing substantially below 10 QL as shown in figure 21(c). The carrier concentrations from BS ($n_{2\text{D-Bulk}}$), 2DEG ($n_{2\text{DEG}}$) and TSS (n_{TSS}) were further separated and it was found that in the region of 5–8 QL, the value of n_{TSS} is larger compared to $n_{2\text{DEG}}$ and $n_{2\text{D-Bulk}}$, indicating a TSS dominated electrical transport in thin Bi_2Se_3 films.

Figure 21(d) presents θ_{sh} as a function of $t_{\text{Bi}_2\text{Se}_3}$ at room temperature by ST-FMR measurements on $\text{Bi}_2\text{Se}_3(t_{\text{Bi}_2\text{Se}_3})/\text{CoFeB}(7\text{ nm})$ bilayers. As $t_{\text{Bi}_2\text{Se}_3}$ is in the range of 5–8 QL, the Bi_2Se_3 films exhibit a giant θ_{sh} of $\sim 1\text{--}1.75$ at room temperature, which further corroborates the TSS dominated transport in thin Bi_2Se_3 film region. In addition, the *interface* SOT efficiency from TSS (λ_{TSS}) using an interface charge current density $J_{\text{C-TSS}}$ (A cm^{-1}) in TSS were estimated for each $t_{\text{Bi}_2\text{Se}_3}$ as

shown by squares in figure 21(e). Furthermore, after subtracting the opposite 2DEG contribution, the intrinsic λ_{TSS} was calculated as 0.8 nm^{-1} for 7, 8 and 10 QL Bi_2Se_3 , as shown by circles, which is similar to recently reported interface SOT efficiency values in $(\text{Bi}_{1-x}\text{Sb}_x)_2\text{Te}_3$ [120].

These results suggest that the BS and 2DEG dilute the TSS contribution and weaken the SOT efficiency in Bi_2Se_3 , and thus by using moderately thin TI films (5-8 QL) one can obtain the TSS dominated SOTs for device applications. In addition, the TSS dominated transport has also been reported recently [123] by changing the Bi_2Se_3 film thickness with a spin pumping technique, which is a reverse process (spin-charge conversion) of ST-FMR.

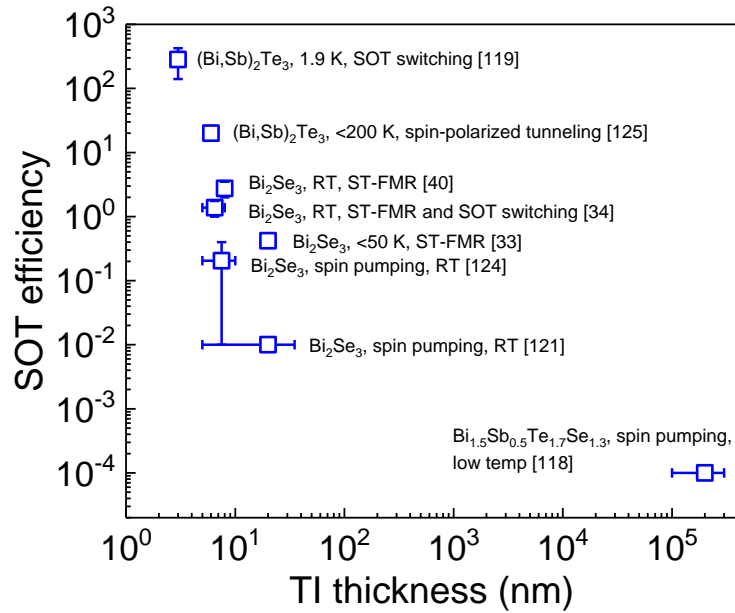


Figure 20. Summary of the SOT efficiencies measured in different TIs with different thicknesses. The materials with corresponding measurement temperature, measurement method and reference are indicated. SOT switching represents the SOT driven magnetization switching.

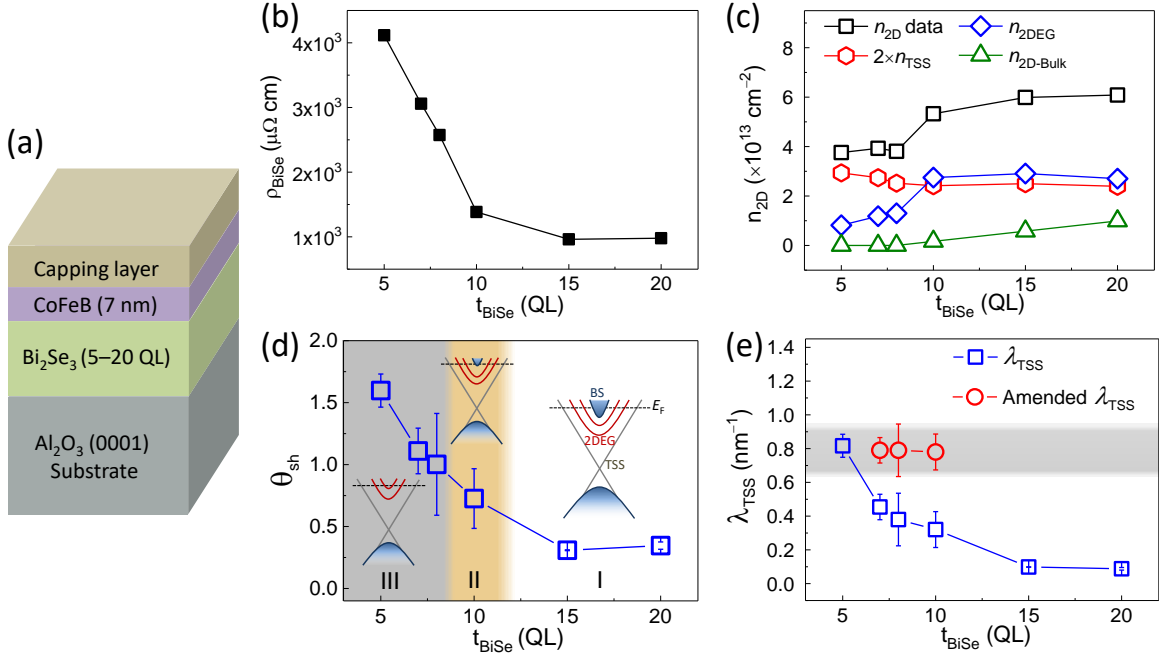


Figure 21. (a) Schematic of the film stack for ST-FMR devices. (b) Bi₂Se₃ thickness dependent resistivity, ρ_{BiSe_3} , in Bi₂Se₃ at room temperature. (c) Estimation of sheet carrier concentration of TSS, 2DEG and bulk channels. (d) θ_{sh} as a function of Bi₂Se₃ thickness at room temperature. Each θ_{sh} represents the averaged value from three devices. Region I, II and III denoted by different colours represent the charge-to-spin conversion dominated by different mechanisms. The inset shows the schematic of the band structure for each region. (e) Interface SOT efficiency, λ_{TSS} (squares), as a function of t_{BiSe_3} at room temperature. Amended interface SOT efficiencies from TSS after excluding the opposite 2DEG contribution for 7, 8 and 10 QL Bi₂Se₃ with circles. Adapted from [34].

By taking advantage of this giant θ_{sh} , SOT driven magnetization switching in the Bi₂Se₃ (8 QL)/Py (6 nm) heterostructures was successfully achieved at room temperature without any external magnetic field [34]. This work makes a substantial improvement in the working temperature of TI based magnetization switching scheme from 1.9 K [119] to 300 K, demonstrating that TI can be an excellent spin generator at room temperature. The critical switching current density J_C in Bi₂Se₃ required for the magnetization switching is extremely low ($\sim 6 \times 10^5 \text{ A/cm}^2$), which is almost two orders of magnitude smaller than that in HMs, such as Pt and

Ta [20-22]. The much lower J_C for magnetization switching using TIs is promising to address the outstanding scalability and power consumption issue in modern magnetic devices. Furthermore, the magnetization switching scheme demonstrated in Ref. [34] does not require an assistive magnetic field, which makes the TI/FM material systems easy to integrate into the well-established industrial technology for magnetic devices. In addition, the room temperature SOT driven magnetization switching has been also observed recently in the Bi_2Se_3 /ferrimagnetic CoTb heterostructures [136] and in the sputtered $\text{Bi}_x\text{Se}_{(1-x)}$ /Ta/CoFeB/Gd/CoFeB heterostructures [137].

7. SOT beyond HMs and TIs

Beyond HMs and TIs, other novel material systems with strong SOC are emerging, which also have potential in the future spintronic applications. The following sections discuss some representative examples, in which the ST-FMR technique was used to evaluate the SOTs (or SOT efficiency), to get insight into the underlying physics of SOTs in these emerging systems.

7.1. Interface between two nonmagnetic materials

The Rashba SOC, which was first discussed in the 2DEG systems with spin degeneration lifting [138], can emerge at the interfaces in a variety of material systems nowadays [139]. The Rashba SOC at an interface is explained as follows. For an interface with inversion symmetry breaking in the direction perpendicular to the interface, an electric field E is produced perpendicular to the interface. An electron moving within this interface with the electric field will experience an effective magnetic field H due to the relativistic corrections, which causes a momentum dependent spin splitting in the bands, analogous to the Zeeman splitting. In the scheme of Rashba SOC, the interaction between the spin polarization $\hat{\sigma}$ and electron momentum k can be expressed by the Hamiltonian $H_R = \alpha_R (k \times \hat{z}) \cdot \hat{\sigma}$, where α_R is the Rashba coefficient, \hat{z} is the unit vector perpendicular to the interface. Figures 22(a) and (b) schematically show the dispersion

curves with spin splitting due to the Rashba SOC at the interface and the corresponding Fermi contours with spin polarization configuration. It is revealed that the spins polarizations are transverse to the electron moving direction. Since the spins have different chiralities in two contours, they compensate each other and give rise to the net spin polarizations, which can be measured in the experiments.

The Rashba SOC at the interface between the HM and FM layer, such as Pt/Co, has been studied previously [20, 72]. Recently, researchers have found that when one nonmagnetic material, such as Bi, Pb or Sb, contacts with other nonmagnetic material, such as Ag, their interface can also exhibit strong interface SOC [140-147]. In 2015, the charge-to-spin conversion induced by the Rashba-Edelstein effect was directly observed at the interface of Bi/Ag [146]. Using a spin-polarized positron beam, they found an opposite surface spin polarization between Bi/Ag/Al₂O₃ and Ag/Bi/Al₂O₃ samples. Subsequently, Jungfleisch *et al.* [147] reported the Rashba-Edelstein-induced-spin driven ST-FMR in Bi/Ag/Py heterostructures. They evaluated the SOT efficiency of the Bi/Ag interface to be ~0.18 using the V_S/V_A ratio method.

Another recent report shows a very large SOT efficiency at the interface between 10 QL Bi₂Se₃ TI materials and nonmagnetic material Ag thin layer at room temperature by ST-FMR measurements [148]. As shown in figure 22(c), from first-principle calculations, it was found that there is a pair of large Rashba splitting bands emerging at the interface between Bi₂Se₃ and Ag. Moreover, the Rashba bands are located outside the TSS linear bands of the Bi₂Se₃ layer, and the Rashba bands have the same net spin polarization direction as the TSS of Bi₂Se₃. As shown in figure 22(d), due to the large interface Rashba SOC at the newly formed Bi₂Se₃/Ag interface, the measured SOT efficiency shows a significant enhancement as the Ag insertion layer thickness increases to ~2 nm and reaches a value of 0.5 for 5 nm Ag. The SOT efficiency in Bi₂Se₃/Ag (5

nm)/CoFeB is ~ 3 times higher than that from sole TSS in Bi₂Se₃/CoFeB at room temperature. The extracted α_R at the Bi₂Se₃/Ag interface has a significant large value about 2.83–3.83 eV Å and this value is similar to that of Bi/Ag previous reported [141]. Furthermore, Rashba-induced magnetization switching in Bi₂Se₃/Ag/Py with a low current density of 5.8×10^5 A/cm² has been demonstrated. As indicated in Section 6.3, the SOT efficiency in Bi₂Se₃/Ag can be further enhanced by decreasing the Bi₂Se₃ thickness to eliminate the bulk contamination and energy consumption will be further decrease for SOT driven magnetization switching. These reports indicate that the nonmagnetic bilayer interface can be designed to provide a large Rashba spin splitting and thus giant SOT efficiency, which has the potential to be used as efficient spin current sources for future spintronic devices.

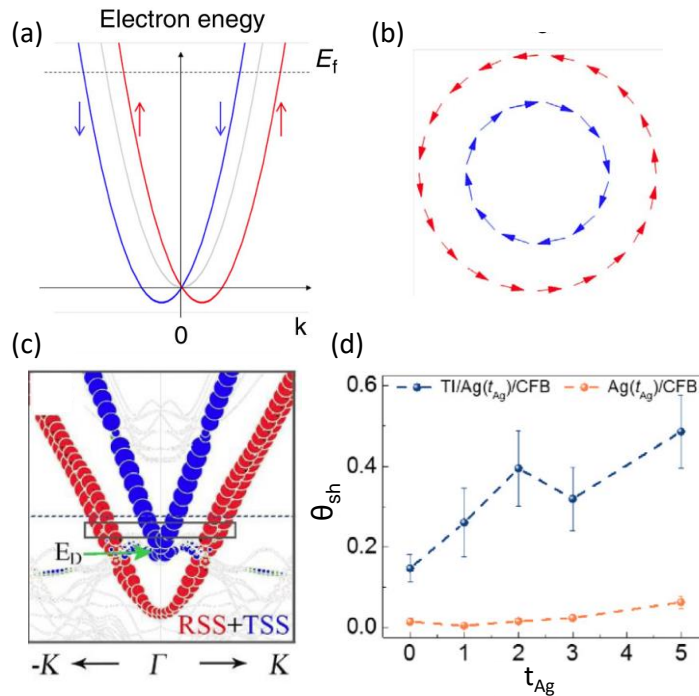


Figure 22. (a) Typical spin-split dispersion curves of a Rashba 2DEG. (b) Fermi contours with spin polarization denoted by the blue and red arrows. Reprinted by permission from Macmillan Publishers Ltd: Nature Communications [143], copyright 2013. (c) Spin-orbit-torque efficiency obtained for both Bi₂Se₃ (10 QL)/Ag (t_{Ag})/CoFeB (7 nm) and Ag (t_{Ag})/CoFeB (7 nm) ST-FMR

devices. (d) The band structure of Bi_2Se_3 (6QL)/Ag (0.95 nm) from first principle calculations. Reprinted with permission from [148]. Copyright (2018) by the American Physical Society.

7.2. Transition-metal dichalcogenides (TMDs)

In the recent years, 2D transition-metal dichalcogenide (TMDs) materials are attracting interests due to the novel physics and potential applications, which were reviewed in Ref. [149]. Since the TMDs display 2D characteristics, the thickness of 2D-TMDs can be reduced as thin as a monolayer. Therefore, TMDs provide an interesting platform to observe exotic interface related phenomena. Since 2016, the 2D-TMDs have been studied as spin current sources for the SOT devices [135, 150-153]. Spin current induced ferromagnetic resonance has been observed in monolayer MoS_2/Py structures [151], where the Py layer was deposited by either magnetron sputtering or e-beam evaporation. It was observed that both τ_{DL} and τ_{FL} in the monolayer MoS_2/Py system were present, with the ratio of $|\tau_{\text{FL}}/\tau_{\text{DL}}| = 0.19$. The observed SOTs were attributed to the interface between the MoS_2 and Py layer. The ratio of $|\tau_{\text{FL}}/\tau_{\text{DL}}|$ in MoS_2/Py is much smaller than that recently reported in the $\text{Bi}_2\text{Se}_3/\text{Py}$ (or CoFeB) systems [33, 40], whose value is in the range of 1.4–2. This implies that the damping-like torque τ_{DL} is much larger than τ_{FL} in MoS_2/Py system. However, the real SOT efficiency of MoS_2/Py bilayer was not evaluated in Ref. [151] and the real SOT efficiency should be estimated by the method only- V_{S} (or τ_{DL}) described in Section 4.2 for proper comparison with other material systems.

Semimetal WTe_2 is also a layered TMD, which has strong SOC [154, 155] and has been reported to possess exotic topological properties [156]. Compared to other TMDs, such as MoS_2 , an interesting property of single crystal WTe_2 is the crystal symmetry. As shown in figure 23(a), the mirror symmetry exists only relative to the bc plane in WTe_2 , and there is no mirror symmetry in the ac plane. Therefore, there is no 180° rotation about the c -axis (perpendicular to the sample plane). Consequently, due to the lack of two-fold rotational symmetry about the c -axis, there is a

possible existence of the out-of-plane damping-like SOT (τ_B) in WTe₂. Recently, MacNeill *et al.* [135] have verified the presence of τ_B in WTe₂/Py bilayer systems by ST-FMR measurements at room temperature shown in figures 23(b) and (c). It was found that when the charge current flows along the *b*-axis with mirror symmetry in a WTe₂ (5.5 nm)/Py (6 nm) device, both the symmetric (V_S) and antisymmetric (V_A) ST-FMR components at different in-plane magnetic field angle φ follow the behaviour of $\cos\varphi \times \sin(2\varphi)$, which is similar to the case of the traditional HM/FM bilayers. However, as the charge current flows along the *a*-axis where mirror symmetry is broken, V_A at different φ exhibits a novel behaviour of $\cos\varphi \times \sin(2\varphi) + \sin(2\varphi)$, indicating the presence of τ_B in WTe₂/Py as shown in figure 23(d). Figure 23(e) shows the SOTs in WTe₂ with different thicknesses ranging from monolayer to ~16 nm [153]. The magnitude of τ_B shows a very weak WTe₂ thickness dependence, suggesting that it is of the interface origin.

Most of the studied interface systems so far only have broken inversion symmetry along their vertical structure, which leads to an in-plane damping-like torque or out-of-plane field-like torque due to Rashba-Edelstein effect at the interface. On the contrary, the results in Ref. [135] demonstrate the in-plane rotational symmetry breaking induced out-of-plane damping-like torque in WTe₂, which is a novel interface related SOT phenomenon and provides a platform for field-free SOT driven magnetization switching of FM with perpendicular magnetic anisotropy (PMA).

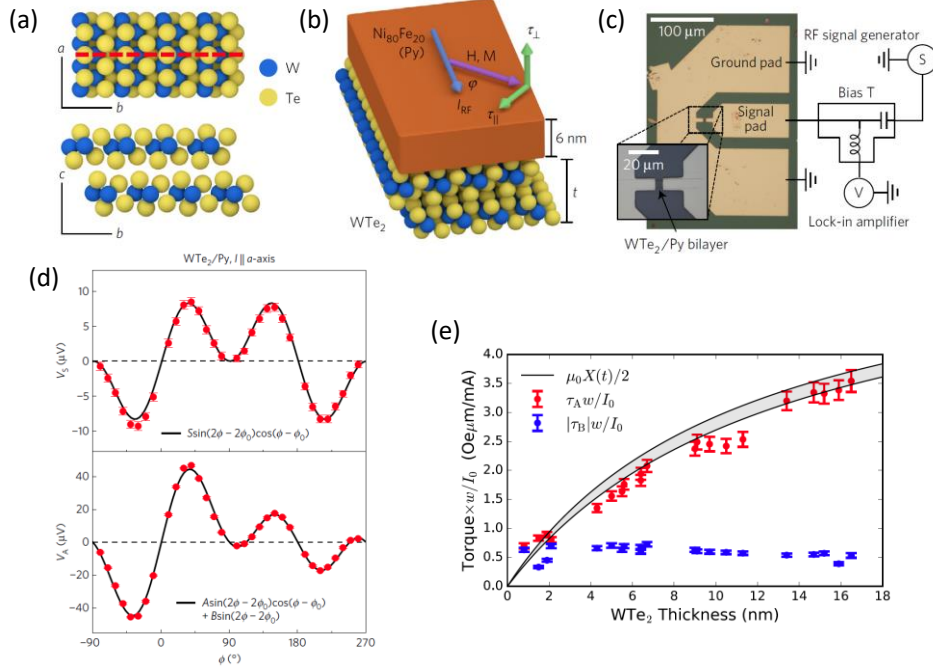


Figure 23. (a) Crystal structure near the surface of WTe_2 . (b) Schematic of the WTe_2/Py sample. (c) The device and the circuit used for ST-FMR measurements. (d) Symmetric and antisymmetric ST-FMR components (V_S and V_A) for a WTe_2 (5.5 nm)/Py (6 nm) device as a function of in-plane magnetic-field angle ϕ denoted in (b). The charge current is applied parallel to the a -axis. The microwave frequency is 9 GHz and the applied microwave power is 5 dBm. Adapted by permission from Macmillan Publishers Ltd: Nature Physics [135], copyright 2016. (e) Out-of-plane damping-like torque (τ_B , blue circles) and out-of-plane field-like torque (τ_A , red circles) per unit interface charge current density (I_0/w) as a function of WTe_2 thickness, where I_0 and w are charge current and channel width, respectively. Reprinted with permission from [153]. Copyright (2017) by the American Physical Society.

7.3. Antiferromagnetic (AFM) materials

Antiferromagnetic materials have zero net magnetization due to the antiparallel alignment of magnetic moments on the adjacent individual atoms. Therefore, the antiferromagnets are difficult to control by external magnetic fields. However, an injected charge current induced internal field can perturb the spin structures and thus magnetic ordering in AFM, as recently reported in different single antiferromagnetic (AFM) materials [157-159]. On the other hand, the devices with AFM/FM heterostructures have also been utilized to realize the external-magnetic-field-free SOT

driven magnetization switching due to the presence of exchange bias [160-163], which breaks the magnetization up-down equivalence in the systems with PMA. Furthermore, a single AFM material itself can also work as a spin current source [48, 160, 164, 165], just like a HM layer. It has been found that the SOT efficiency of the single AFMs, such as PtMn, IrMn, is in the same order of Pt [160, 166, 167].

Interestingly, it was also found that there is an anisotropy of the ST-FMR results from epitaxial PtMn [48] and IrMn₃ [165] AFM films. For PtMn epitaxial films [48], the modulation of ST-FMR linewidth (MOD) is more significant along the *a*-axis than *c*-axis PtMn (10 nm)/Cu (1 nm)/Py (5 nm) samples as shown in the figures 24(a) and (b), indicating the large SOT efficiency in *a*-axis PtMn films. A further only- V_S ST-FMR analysis method yields a SOT efficiency of ~ 0.048 for *c*-axis PtMn and ~ 0.089 for *a*-axis PtMn. For the case of epitaxial IrMn₃/Py bilayer devices [165], a similar anisotropic behaviour was found from ST-FMR measurements in the SOT efficiency with respect to the IrMn₃ crystal orientations. As shown in figure 24(c), the SOT efficiency is much larger (~ 0.2) in (001)-oriented single-crystalline IrMn₃ than that in either (111)-oriented or polycrystalline-oriented films. Moreover, after perpendicular field annealing, an enhanced SOT efficiency up to ~ 0.35 in (001)-oriented IrMn₃ thin films was demonstrated. Both works discussed that the observed anisotropic SOT efficiency in PtMn or IrMn₃ epitaxial films originates from the intrinsic SHE, which was further corroborated with the first-principles calculations.

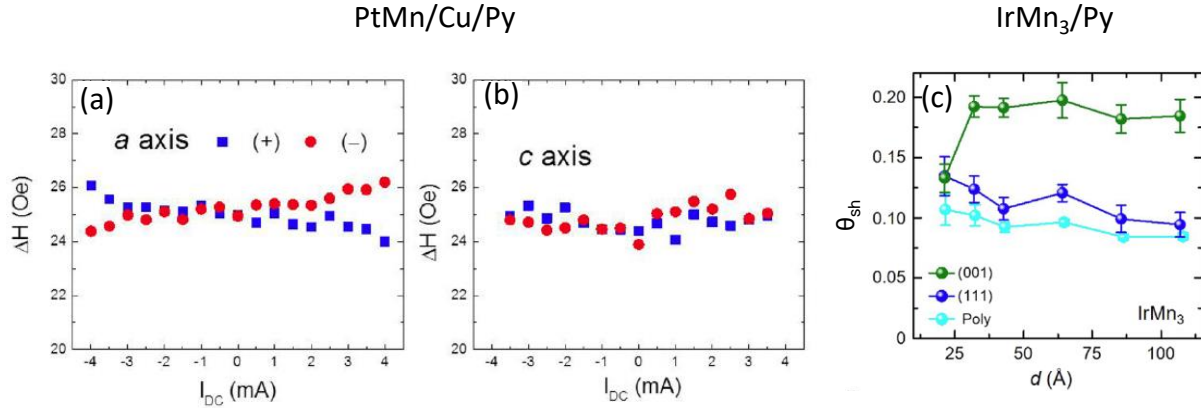


Figure 24. Measured resonance linewidth versus dc-bias current by ST-FMR measurements at 5 GHz for (a) *a*- and (b) *c*-axis PtMn (10 nm)/Cu (1 nm)/Py (5 nm). Reprinted with permission from [48]. Copyright (2015) by the American Physical Society. (c) SOT efficiency as a function of IrMn₃ thickness for different crystal orientation films, i.e. (001)-oriented (olive circles), (111)-oriented (blue circles), and polycrystalline-oriented (cyan circles). Reprinted from [165]. 2016 © The Authors, some rights reserved; exclusive licensee American Association for the Advancement of Science. Distributed under a Creative Commons Attribution NonCommercial License 4.0 (CC BY-NC).

7.4. 2DEG in oxide materials

Recent advances in film growth and synthesis techniques have enabled the growth of high quality oxide heterostructures with very smooth interfaces. This allows for engineering novel electronic properties at the oxide interfaces [168]. One of the central oxide material systems is the interface between two wide-band-gap insulators, SrTiO₃ (STO) and LaAlO₃ (LAO) as a 2DEG is formed at the interface and possesses exotic properties including superconductivity [169, 170] and magnetism [171-173]. Further, due to the broken interfacial inversion symmetry, the 2DEG confined in the vicinity of polar (LAO)/non-polar (STO) interface experiences a strong electric field directed perpendicular to the conduction plane [174]. Consequently, the LAO/STO interface possesses a strong Rashba SOC that leads to a strong coupling between the orbital and spin degrees of freedom. Due to the dielectric properties of STO, the strength of the Rashba SOC is tunable by

applying an external gate voltage [175].

The presence of strong Rashba SOC in the d -bands of the 2DEG at the STO/LAO interface has been reported in various earlier studies [175-177]. Further, the Rashba SOC allows for generation of spin accumulation in the LAO/STO interface when a charge current flows in the 2DEG [138, 178]. Subsequently, the existence of current induced SOTs at the STO/LAO interface has been verified experimentally by angular dependent magnetoresistance measurements [179]. Recently, Wang *et al.*[180] have experimentally shown a giant room temperature charge-to-spin conversion efficiency (i.e. θ_{sh}) in the STO/LAO/CoFeB structure by the ST-FMR technique shown in figure 25(a). The θ_{sh} value was estimated to be ~ 6.3 at room temperature denoted by squares in figure 25(b), which is almost two orders of magnitude larger than that in HMs, such as Pt and Ta [21, 25]. However, the θ_{sh} decreases rapidly as the temperature decreases to ~ 150 K. Finally, it becomes negligible at ~ 50 K. From the temperature dependent θ_{sh} , it was suggested that inelastic tunneling via localized states, such as oxygen vacancies in the LAO band gap, accounts for the spin transmission through the LAO layer, as schematically shown in the inset of figure 25(b).

In addition to the ST-FMR measurements, a spin-to-charge conversion efficiency at the STO/LAO interface has been also reported by the spin pumping technique [181-183]. Additionally, a long spin diffusion length over 300 nm in the STO/LAO 2DEG channel has been reported [184, 185]. Therefore, the oxide materials, such as STO/LAO heterostructures, can enable potential applications in the oxide based spintronic devices.

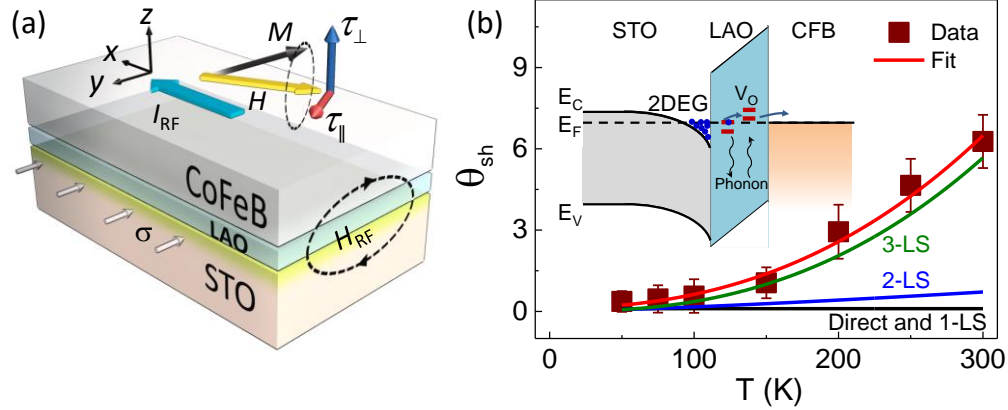


Figure 25. (a) Illustration of a STO/LAO/CoFeB ST-FMR device with the SOT induced magnetization dynamics. (b) SOT efficiency, θ_{sh} , as a function of temperature (squares) and the fit (red line). The inset is the schematic of the spin-polarized electron inelastic tunneling process via the localized states (LS), such as oxygen vacancies, V_O . The fitting lines with the black, blue and green colours denote the contributions of the respective direct elastic tunneling & 1- localized state (LS), 2-LS and 3-LS chains. Reprinted with permission from [180]. Copyright (2017) American Chemical Society.

7.5. Nonmagnetic oxidized materials

In conventional HMs, the reported largest SOT efficiency is ~ 0.3 observed in β -phase W [35]. However, the α -phase W exhibits a much smaller SOT efficiency. Therefore, the SOTs can be controlled via the HM microstructure engineering. Recently, it has been reported that the SOT efficiency can be significantly enhanced in a W/Py bilayer by oxygen incorporation in the W layer [186]. It was found that as the oxygen concentration increases, the grain size decreases, but the resistivity increases, in which β -phase W is well stabilized. Consequently, an enhanced SOT efficiency up to ~ 0.5 was achieved with an oxygen concentration of 12.1% compared to ~ 0.14 for zero oxygen incorporation. For higher oxygen incorporations up to 44%, the bulk properties further changed, however the SOT efficiency showed a very weak oxygen concentration dependence, suggesting that the mechanism responsible for the observed highly SOT efficiency may originate from the W (oxygen)/Py interface.

Recently, An *et al.* [187] found that by naturally oxidizing a light metal Cu with very weak SOC, the SOT efficiency in a Cu/Py bilayer was enhanced to be ~ 0.08 , which is similar as Pt and more than two orders of magnitude larger than that in pure Cu. These results indicate that engineering materials with oxidization opens an intriguing path to enhance the SOT and realize efficient spintronic devices [188].

8. Summary and Perspectives

In this review, we first described the ST-FMR technique, including two ST-FMR setups and three ST-FMR analysis methods. As ST-FMR is a high frequency measurement in the GHz frequency range, several aspects should be carefully considered during the ST-FMR measurements and data analysis, such as the symmetric CPW design, impedance matching, rf power absorption and device current correction as well as possible contamination considerations (field-like torque from the interface effect and spin pumping). Then the latest SOT research progresses using ST-FMR are presented in diverse materials including normal HMs and alloys, TIs, 2D materials, interfaces with strong Rashba SOC, AFM materials, 2DEG in oxide materials as well as nonmagnetic oxidized materials. We find that the ST-FMR measurement is a powerful technique to determine the SOT efficiency including the recently observed out-of-plane damping-like SOT efficiency in a WTe_2 Weyl semimetal. We hope this review can further promote the ST-FMR technique in fundamental SOT researches as well as exploiting novel materials for future spin-based device applications.

In figure 26 we have summarized the representative SOT efficiencies in various materials as well as the power consumption for switching an unit magnetization of a FM layer which is proportional to $1/(\sigma \times (\theta_{sh})^2)$ [136]. Here we assume that the switching time is same in all the materials for simplicity. It shows that the TI materials generally show a larger SOT efficiency as

well as low power due to the efficient charge-spin conversion in the spin-momentum-locked surface states compared to HMs. Some other materials, apart from HMs and TIs, also exhibit a high performance in terms of both SOT efficiency and power consumption and thus are worth for further studies.

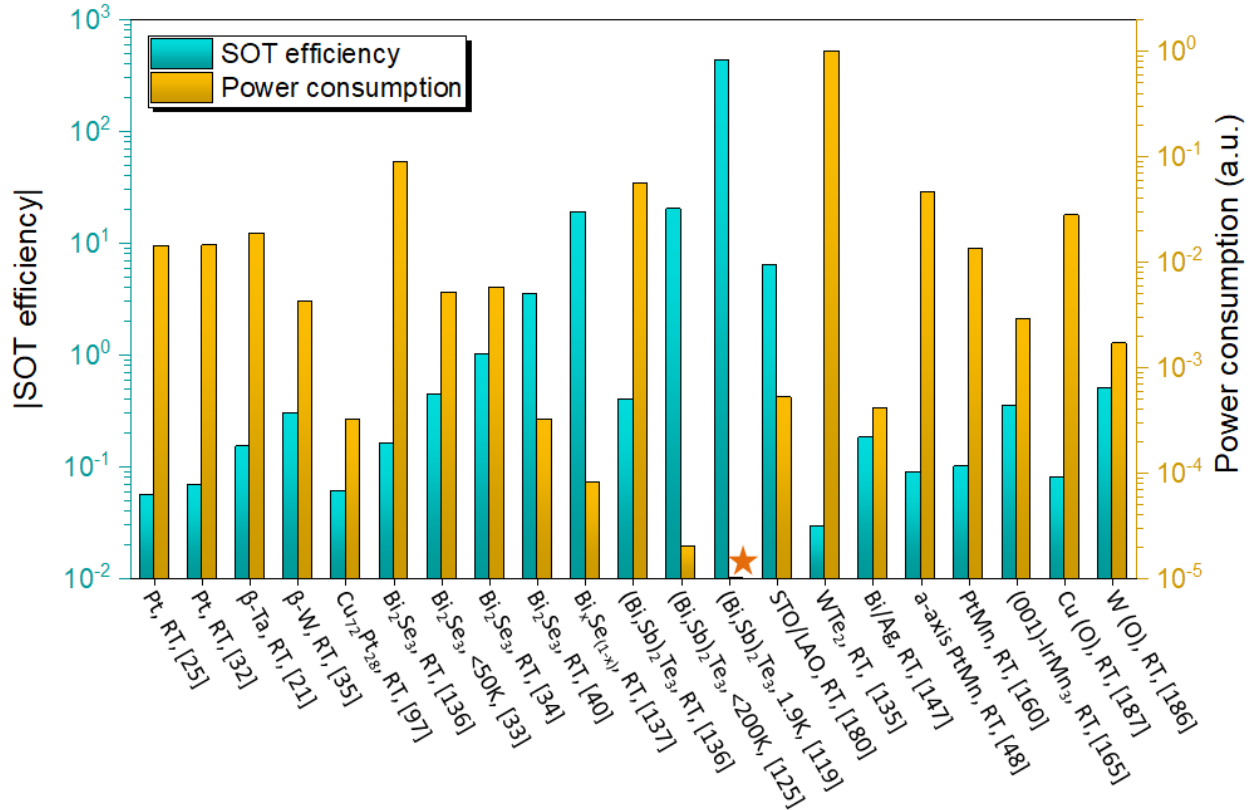


Figure 26. Summary of the SOT efficiencies (left y-axis) and normalized power consumption of a variety of materials (right y-axis). The x-axis denotes the materials with their corresponding measurement temperature and reference. RT means room temperature. The Bi_xSe_(1-x) represents the film grown by the magnetron sputtering, the STO/LAO represents SrTiO₃/LaAlO₃ bilayer, and Cu (O) and W(O) represent the metal films with oxygen incorporation. The star represents an extremely small normalized power consumption value ($\approx 5.5 \times 10^{-8}$) for (Bi,Sb)₂Te₃ at a temperature of 1.9 K. The effective conductivity σ ($\sim 0.17 \mu\Omega^{-1}\cdot\text{cm}^{-1}$) of Bi 4 (nm)/Ag (8 nm) bilayer, used for the power consumption estimation, is calculated using a parallel circuit model with the given conductivity values of $\sim 2.1 \times 10^{-4} \mu\Omega^{-1}\cdot\text{cm}^{-1}$ (for Bi) and $\sim 0.25 \mu\Omega^{-1}\cdot\text{cm}^{-1}$ (for Ag). The σ ($\sim 0.0125 \mu\Omega^{-1}\cdot\text{cm}^{-1}$) of Cu (O) layer, used for the power consumption estimation, is

extracted from the figure 1(b) in Ref. [187] by using the given value of the pure Cu conductivity ($\sim 0.025 \mu\Omega^{-1}\cdot\text{cm}^{-1}$).

Figure 27 shows the correlation of SOT efficiency and power consumption for different materials, obtained by reorganising and grouping the data in figure 26 based on their corresponding material system. Overall, we find that the TI materials (wrapped by the red dashed curve) shows a better performance in terms of the SOT efficiency and the power consumption even though the values are scattered due to the influence of conducting bulk. The HMs and their alloys (wrapped by the dashed blue curve) possess a similar orders of SOT efficiency and comparable power consumptions as the AFM systems but are inferior to the TI systems. Finally, the Weyl semimetal WTe_2 seems to show a higher power consumption based on the single report in Ref [135]. Since, Weyl semimetals are a very interesting topological materials, more research works are expected in the near future and one can obtain a more conclusive view about the performance of Weyl semimetals in the power consumption and SOT driven switching efficiency.

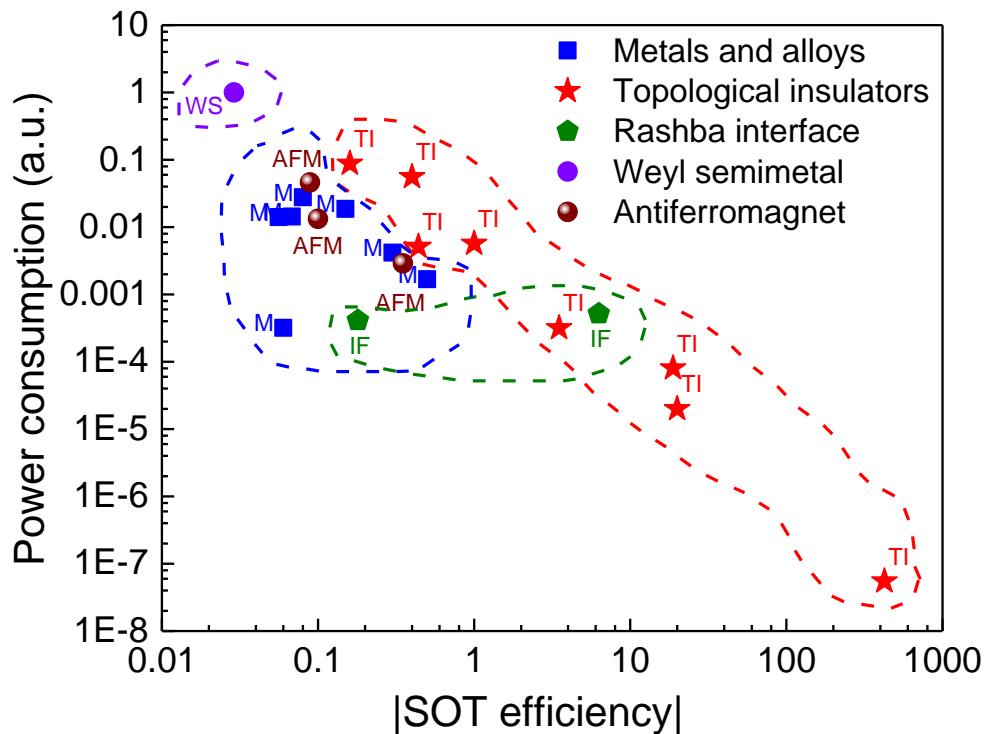


Figure 27. Summary of the normalized power consumption as a function of SOT efficiencies for a variety of materials. ‘Metals and alloys’ represent Pt, Ta, W, and CuPt alloy and nonmagnetic oxidized materials, ‘Topological insulators’ represent Bi_2Se_3 and $(\text{Bi,Sb})_2\text{Te}_3$, ‘Rashba interface’ includes STO/LAO interface and Bi/Ag interface, ‘Weyl semimetal’ means WTe_2 , and ‘Antiferromagnet’ includes PtMn and IrMn_3 .

Moving towards to the real SOT applications, many reports recently have studied the SOT devices in the nanosecond (ns) or even picosecond (ps) regime [104, 108, 189-192]. A very high efficient SOT driven magnetization switching has been realized recently [191], where the switching energy is only about 60 fJ for each bit writing with the current $\sim 120 \mu\text{A}$ and time of 1.2 ns. The energy consumption for each bit writing is much smaller than the values known in STT driven magnetization switching, which is between $\sim 150 \text{ fJ}$ to $\sim 4 \text{ pJ}$ [193-195]. Therefore, the SOT devices are promising and potential candidates for the future high efficient spintronic devices. Thus, the exploration of novel materials with even higher SOT efficiency will be of great importance for the future spin-based device applications and, for this purpose, the ST-FMR can be an easy and a powerful technique.

So far, we have seen that the origins of the SOT can be from the bulk, surface and/or interface in a variety of materials. Based upon the origins of the SOT, the material systems will show different thickness dependent behaviours. Figure 28 shows the schematic of the SOT efficiency as a function of thickness in representative TI material Bi_2Se_3 , HM material Pt and Weyl semimetal WTe_2 . For HMs (blue curve), the dominant mechanism for the SOT is SHE, which is a bulk property. Therefore, the SOT efficiency in HMs usually increases and then saturates as HMs thickness increases. The thickness corresponding to the saturation point of SOT efficiency is correlated to the spin diffusion length in HMs. For the TIs (red curve), the TSS serve as the main mechanism for the SOT and should have almost a constant SOT efficiency against the TI thickness as reported in Ref. [34] (also see figure 21(e)). However, as mentioned in Section 6.3, the

contamination from the conducting bulk might be unavoidable. Consequently, the SOT efficiency shows much larger values as the TI thickness becomes thinner as TSS becomes dominant. As reported in WTe₂ [153], the out-of-plane damping-like SOT efficiency, due to a broken lateral mirror symmetry, remains almost constant with respect to the WTe₂ thickness, which is claimed to arise from interface mechanisms. The weak thickness dependence is illustrated by the green curve in figure 28. Therefore, the thickness dependent SOT efficiency (or SOT) measurements by ST-FMR or even other reliable techniques are very useful to get insight into the underlying physics of an emerging materials in the future.

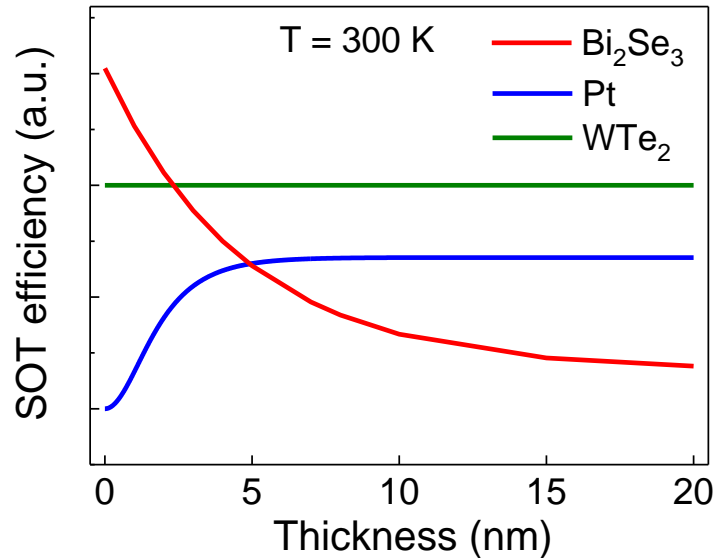


Figure 28. Schematic of the SOT efficiency as a function of thickness in representative materials Bi₂Se₃, Pt and WTe₂, replotted by using the data from figure 21(d) and (e), 8(a) and 23(e) in this review article, respectively.

The central physical effect used in the ST-FMR measurement can be further explored besides the GMR, tunneling magnetoresistance (TMR) or AMR rectification [196] in the present ST-FMR devices. The other magnetoresistance effects, such as the SMR, or Hall effects such as the anomalous Hall effect (AHE) and planar Hall effect (PHE), with both in-plane and out-of-plane

measurement schemes, might also be developed in the near future to extend the ST-FMR technique to different material systems, especially for the materials with perpendicular magnetic anisotropy. Meanwhile, the ST-FMR analysis theory should be also modified accordingly. Subsequently, the SOT efficiency from ST-FMR measurements can provide a much better comparison with that from other measurements techniques. Good examples for this are the recent reports where the ST-FMR rectification signals were obtained based on the SMR effect in the Pt/yttrium iron garnet (YIG) magnetic insulator bilayer [197-199].

In addition, ST-FMR measurements on nontrivial topological materials, such as Weyl semimetals (WTe₂ [154] or MoTe₂ [200]), can be an future interesting topic. It would be significant discovery if one can observe the Fermi-arc surface states and/or Weyl node related topological phenomena using the ST-FMR technique. Apart from the above materials, the AFM materials are interesting to be further explored using ST-FMR measurements, as the AFMs are predicted to have a long spin coherence length due to the staggered spin order on an atomic scale and thus possess possible bulk-torque-like characteristics [201-203].

Besides the applications in the SOT studies, it has been demonstrated recently that TMR based ST-FMR devices have a very high efficiency in converting an rf frequency signal to dc signal, even better than the conventional Schottky diode [15, 204-206]. This high rectification efficiency of TMR based ST-FMR devices can be utilized for wireless energy harvesting that is becoming more relevant to the technologies such as internet of things (IoT).

Acknowledgments

This work was partially supported by the National Research Foundation (NRF), Prime Minister's Office, Singapore, under its Competitive Research Programme (CRP Award No. NRFCRP12-2013-01), NRF Industry-IHL Partnership (IIP) grant (R-263-000-C26-281), and A*STAR's Pharos Programme on Topological Insulators.

References:

- [1] Brataas A, Kent A D and Ohno H 2012 Current-induced torques in magnetic materials *Nat. Mater.* **11** 372
- [2] Jungwirth T, Wunderlich J and Olejník K 2012 Spin Hall effect devices *Nat. Mater.* **11** 382
- [3] Sander D, Valenzuela S, Makarov D, Marrows C, Fullerton E, Fischer P, McCord J, Vavassori P, Mangin S and Pirro P 2017 The 2017 Magnetism Roadmap *J. Phys. D: Appl. Phys.* **50** 363001
- [4] Yuasa S and Djayaprawira D 2007 Giant tunnel magnetoresistance in magnetic tunnel junctions with a crystalline MgO (0 0 1) barrier *J. Phys. D: Appl. Phys.* **40** R337
- [5] Ikeda S, Miura K, Yamamoto H, Mizunuma K, Gan H, Endo M, Kanai S, Hayakawa J, Matsukura F and Ohno H 2010 A perpendicular-anisotropy CoFeB–MgO magnetic tunnel junction *Nat. Mater.* **9** 721-4
- [6] Thomas L, Jan G, Zhu J, Liu H, Lee Y-J, Le S, Tong R-Y, Pi K, Wang Y-J and Shen D 2014 Perpendicular spin transfer torque magnetic random access memories with high spin torque efficiency and thermal stability for embedded applications *J. Appl. Phys.* **115** 172615
- [7] Han X, Wen Z, Wang Y, Liu H, Wei H and Liu D 2011 Nanoelliptic ring-shaped magnetic tunnel junction and its application in MRAM design with spin-polarized current switching *IEEE Trans. Magn.* **47** 2957-61
- [8] Griffiths J H E 1946 Anomalous High-frequency Resistance of Ferromagnetic Metals *Nature* **158** 670
- [9] Kittel C 1948 On the theory of ferromagnetic resonance absorption *Phys. Rev.* **73** 155
- [10] Slonczewski J C 1996 Current-driven excitation of magnetic multilayers *J. Magn. Magn. Mater.* **159** L1-L7
- [11] Berger L 1996 Emission of spin waves by a magnetic multilayer traversed by a current *Phys. Rev. B* **54** 9353
- [12] Katine J, Albert F, Buhrman R, Myers E and Ralph D 2000 Current-driven magnetization reversal and spin-wave excitations in Co/Cu/Co pillars *Phys. Rev. Lett.* **84** 3149
- [13] Huai Y, Albert F, Nguyen P, Pakala M and Valet T 2004 Observation of spin-transfer switching in deep submicron-sized and low-resistance magnetic tunnel junctions *Appl. Phys. Lett.* **84** 3118-20
- [14] Mangin S, Ravelosona D, Katine J, Carey M, Terris B and Fullerton E E 2006 Current-induced magnetization reversal in nanopillars with perpendicular anisotropy *Nature Materials* **5** 210-5
- [15] Tulapurkar A, Suzuki Y, Fukushima A, Kubota H, Maehara H, Tsunekawa K, Djayaprawira D, Watanabe N and Yuasa S 2005 Spin-torque diode effect in magnetic tunnel junctions *Nature* **438** 339-42
- [16] Sankey J, Braganca P, Garcia A, Krivorotov I, Buhrman R and Ralph D 2006 Spin-transfer-driven ferromagnetic resonance of individual nanomagnets *Phys. Rev. Lett.* **96** 227601
- [17] Fuchs G, Sankey J, Pribiag V, Qian L, Braganca P, Garcia A, Ryan E, Li Z-P, Ozatay O and Ralph D 2007 Spin-torque ferromagnetic resonance measurements of damping in nanomagnets *Appl. Phys. Lett.* **91** 062507
- [18] Sankey J C, Cui Y-T, Sun J Z, Slonczewski J C, Buhrman R A and Ralph D C 2008 Measurement of the spin-transfer-torque vector in magnetic tunnel junctions *Nat. Phys.* **4** 67-71
- [19] Kato Y, Myers R, Gossard A and Awschalom D 2004 Observation of the spin Hall effect in semiconductors *science* **306** 1910-3
- [20] Miron I M, Garello K, Gaudin G, Zermatten P-J, Costache M V, Auffret S, Bandiera S, Rodmacq B, Schuhl A and Gambardella P 2011 Perpendicular switching of a single ferromagnetic layer induced by in-plane current injection *Nature* **476** 189-93
- [21] Liu L, Pai C-F, Li Y, Tseng H W, Ralph D C and Buhrman R A 2012 Spin-Torque Switching with the Giant Spin Hall Effect of Tantalum *Science* **336** 555
- [22] Liu L, Lee O J, Gudmundsen T J, Ralph D C and Buhrman R A 2012 Current-Induced Switching of Perpendicularly Magnetized Magnetic Layers Using Spin Torque from the Spin Hall Effect *Phys. Rev.*

- Let.* **109** 096602
- [23] Demidov V E, Urazhdin S, Ulrichs H, Tiberkevich V, Slavin A, Baither D, Schmitz G and Demokritov S O 2012 Magnetic nano-oscillator driven by pure spin current *Nat. Mater.* **11** 1028-31
- [24] Seo S-M, Kim K-W, Ryu J, Lee H-W and Lee K-J 2012 Current-induced motion of a transverse magnetic domain wall in the presence of spin Hall effect *Appl. Phys. Lett.* **101** 022405
- [25] Liu L, Moriyama T, Ralph D C and Buhrman R A 2011 Spin-Torque Ferromagnetic Resonance Induced by the Spin Hall Effect *Phys. Rev. Lett.* **106** 036601
- [26] Landau L and Lifshitz E 1935 On the Theory of the disperison of magnetic permeability in ferromagnetic bodies *Phys. Z. Sowjetunion* **169** 14
- [27] Zhang S, Levy P and Fert A 2002 Mechanisms of spin-polarized current-driven magnetization switching *Physical review letters* **88** 236601
- [28] Gui Y, Mecking N, Zhou X, Williams G and Hu C-M 2007 Realization of a room-temperature spin dynamo: The spin rectification effect *Phys. Rev. Lett.* **98** 107602
- [29] Wirthmann A, Fan X, Gui Y, Martens K, Williams G, Dietrich J, Bridges G and Hu C-M 2010 Direct phase probing and mapping via spintronic michelson interferometry *Phys. Rev. Lett.* **105** 017202
- [30] Harder M, Cao Z, Gui Y, Fan X and Hu C-M 2011 Analysis of the line shape of electrically detected ferromagnetic resonance *Phys. Rev. B* **84** 054423
- [31] Landau L D and Lifshitz E M *Mechanics, 2nd ed. (Pergamon, Oxford, 1969)*
- [32] Wang Y, Deorani P, Qiu X, Kwon J H and Yang H 2014 Determination of intrinsic spin Hall angle in Pt *Appl. Phys. Lett.* **105** 152412
- [33] Wang Y, Deorani P, Banerjee K, Koirala N, Brahlek M, Oh S and Yang H 2015 Topological Surface States Originated Spin-Orbit Torques in Bi₂Se₃ *Phys. Rev. Lett.* **114** 257202
- [34] Wang Y, Zhu D, Wu Y, Yang Y, Yu J, Ramaswamy R, Mishra R, Shi S, Elyasi M, Teo K-L, Wu Y and Yang H 2017 Room temperature magnetization switching in topological insulator-ferromagnet heterostructures by spin-orbit torques *Nat. Commun.* **8** 1364
- [35] Pai C-F, Liu L, Li Y, Tseng H, Ralph D and Buhrman R 2012 Spin transfer torque devices utilizing the giant spin Hall effect of tungsten *Appl. Phys. Lett.* **101** 122404
- [36] Thiaville A and Nakatani Y 2008 Electrical rectification effect in single domain magnetic microstrips: A micromagnetics-based analysis *J. Appl. Phys.* **104** 093701
- [37] Kubota H, Fukushima A, Yakushiji K, Nagahama T, Yuasa S, Ando K, Maehara H, Nagamine Y, Tsunekawa K and Djayaprawira D D 2008 Quantitative measurement of voltage dependence of spin-transfer torque in MgO-based magnetic tunnel junctions *Nat. Phys.* **4** 37
- [38] Skinner T, Wang M, Hindmarch A, Rushforth A, Irvine A, Heiss D, Kurebayashi H and Ferguson A 2014 Spin-orbit torque opposing the Oersted torque in ultrathin Co/Pt bilayers *Appl. Phys. Lett.* **104** 062401
- [39] Allen G, Manipatruni S, Nikonov D E, Doczy M and Young I A 2015 Experimental demonstration of the coexistence of spin Hall and Rashba effects in β - tantalum/ferromagnet bilayers *Phys. Rev. B* **91** 144412
- [40] Mellnik A R, Lee J S, Richardella A, Grab J L, Mintun P J, Fischer M H, Vaezi A, Manchon A, Kim E A, Samarth N and Ralph D C 2014 Spin-transfer torque generated by a topological insulator *Nature* **511** 449
- [41] Petit S, Baraduc C, Thirion C, Ebels U, Liu Y, Li M, Wang P and Dieny B 2007 Spin-Torque Influence on the High-Frequency Magnetization Fluctuations in Magnetic Tunnel Junctions *Phys. Rev. Lett.* **98** 077203
- [42] Wang C, Cui Y-T, Katine J A, Buhrman R A and Ralph D C 2011 Time-resolved measurement of spin-transfer-driven ferromagnetic resonance and spin torque in magnetic tunnel junctions *Nat. Phys.* **7** 496-501
- [43] Ando K, Takahashi S, Harii K, Sasage K, Ieda J, Maekawa S and Saitoh E 2008 Electric manipulation of

- spin relaxation using the spin Hall effect *Phys. Rev. Lett.* **101** 036601
- [44] Kasai S, Kondou K, Sukegawa H, Mitani S, Tsukagoshi K and Otani Y 2014 Modulation of effective damping constant using spin Hall effect *Appl. Phys. Lett.* **104** 092408
- [45] Ganguly A, Kondou K, Sukegawa H, Mitani S, Kasai S, Niimi Y, Otani Y and Barman A 2014 Thickness dependence of spin torque ferromagnetic resonance in Co₇₅Fe₂₅/Pt bilayer films *Appl. Phys. Lett.* **104** 072405
- [46] Nan T, Emori S, Boone C T, Wang X, Oxholm T M, Jones J G, Howe B M, Brown G J and Sun N X 2015 Comparison of spin-orbit torques and spin pumping across NiFe/Pt and NiFe/Cu/Pt interfaces *Phys. Rev. B* **91** 214416
- [47] Tiwari D, Behera N, Kumar A, Dürrenfeld P, Chaudhary S, Pandya D, Åkerman J and Muduli P 2017 Antidamping spin-orbit torques in epitaxial-Py (100)/β-Ta *Appl. Phys. Lett.* **111** 232407
- [48] Zhang W, Jungfleisch M B, Freimuth F, Jiang W, Sklenar J, Pearson J E, Ketterson J B, Mokrousov Y and Hoffmann A 2015 All-electrical manipulation of magnetization dynamics in a ferromagnet by antiferromagnets with anisotropic spin Hall effects *Phys. Rev. B* **92** 144405
- [49] Hirsch J E 1999 Spin Hall Effect *Phys. Rev. Lett.* **83** 1834-7
- [50] Zhang S 2000 Spin Hall Effect in the Presence of Spin Diffusion *Phys. Rev. Lett.* **85** 393-6
- [51] Hoffmann A 2013 Spin Hall Effects in Metals *IEEE Trans. Magn.* **49** 5172-93
- [52] Sinova J, Valenzuela S O, Wunderlich J, Back C H and Jungwirth T 2015 Spin Hall effects *Rev. Mod. Phys.* **87** 1213-60
- [53] D'yakonov M and Perel V 1971 Possibility of orienting electron spins with current *Soviet Journal of Experimental and Theoretical Physics Letters* **13** 467
- [54] Valenzuela S O and Tinkham M 2006 Direct electronic measurement of the spin Hall effect *Nature* **442** 176
- [55] Vila L, Kimura T and Otani Y 2007 Evolution of the spin Hall effect in Pt nanowires: size and temperature effects *Phys. Rev. Lett.* **99** 226604
- [56] Seki T, Hasegawa Y, Mitani S, Takahashi S, Imamura H, Maekawa S, Nitta J and Takanashi K 2008 Giant spin Hall effect in perpendicularly spin-polarized FePt/Au devices *Nat. Mater.* **7** 125-9
- [57] Saitoh E, Ueda M, Miyajima H and Tataru G 2006 Conversion of spin current into charge current at room temperature: Inverse spin-Hall effect *Appl. Phys. Lett.* **88** 182509
- [58] Nakayama H, Althammer M, Chen Y-T, Uchida K, Kajiwara Y, Kikuchi D, Ohtani T, Geprägs S, Opel M and Takahashi S 2013 Spin Hall magnetoresistance induced by a nonequilibrium proximity effect *Phys. Rev. Lett.* **110** 206601
- [59] Kondou K, Sukegawa H, Mitani S, Tsukagoshi K and Kasai S 2012 Evaluation of spin Hall angle and spin diffusion length by using spin current-induced ferromagnetic resonance *Appl. Phys. Express* **5** 073002
- [60] Liu L, Buhrman R and Ralph D 2011 Review and analysis of measurements of the spin Hall effect in platinum *arXiv preprint arXiv:1111.3702*
- [61] Morota M, Niimi Y, Ohnishi K, Wei D, Tanaka T, Kontani H, Kimura T and Otani Y 2011 Indication of intrinsic spin Hall effect in 4 d and 5 d transition metals *Phys. Rev. B* **83** 174405
- [62] Feng Z, Hu J, Sun L, You B, Wu D, Du J, Zhang W, Hu A, Yang Y and Tang D 2012 Spin Hall angle quantification from spin pumping and microwave photoresistance *Phys. Rev. B* **85** 214423
- [63] Nakayama H, Ando K, Harii K, Yoshino T, Takahashi R, Kajiwara Y, Uchida K-i, Fujikawa Y and Saitoh E 2012 Geometry dependence on inverse spin Hall effect induced by spin pumping in Ni₈₁Fe₁₉/Pt films *Phys. Rev. B* **85** 144408
- [64] Vlamincik V, Pearson J E, Bader S D and Hoffmann A 2013 Dependence of spin-pumping spin Hall effect measurements on layer thicknesses and stacking order *Phys. Rev. B* **88** 064414
- [65] Vlietstra N, Shan J, Castel V, Van Wees B and Youssef J B 2013 Spin-Hall magnetoresistance in platinum on yttrium iron garnet: Dependence on platinum thickness and in-plane/out-of-plane

- magnetization *Phys. Rev. B* **87** 184421
- [66] Zhang W, Vlamincik V, Pearson J E, Divan R, Bader S D and Hoffmann A 2013 Determination of the Pt spin diffusion length by spin-pumping and spin Hall effect *Appl. Phys. Lett.* **103** 242414
- [67] Althammer M, Meyer S, Nakayama H, Schreier M, Altmannshofer S, Weiler M, Huebl H, Geprägs S, Opel M and Gross R 2013 Quantitative study of the spin Hall magnetoresistance in ferromagnetic insulator/normal metal hybrids *Phys. Rev. B* **87** 224401
- [68] Weiler M, Althammer M, Schreier M, Lotze J, Pernpeintner M, Meyer S, Huebl H, Gross R, Kamra A and Xiao J 2013 Experimental test of the spin mixing interface conductivity concept *Phys. Rev. Lett.* **111** 176601
- [69] Obstbaum M, Härtinger M, Bauer H, Meier T, Swientek F, Back C and Woltersdorf G 2014 Inverse spin Hall effect in Ni₈₁Fe₁₉/normal-metal bilayers *Phys. Rev. B* **89** 060407
- [70] Bass J and Pratt Jr W P 2007 Spin-diffusion lengths in metals and alloys, and spin-flipping at metal/metal interfaces: an experimentalist's critical review *J. Phys. Condens. Matter* **19** 183201
- [71] Niimi Y, Wei D, Idzuchi H, Wakamura T, Kato T and Otani Y 2013 Experimental verification of comparability between spin-orbit and spin-diffusion lengths *Phys. Rev. Lett.* **110** 016805
- [72] Mihai Miron I, Gaudin G, Auffret S, Rodmacq B, Schuhl A, Pizzini S, Vogel J and Gambardella P 2010 Current-driven spin torque induced by the Rashba effect in a ferromagnetic metal layer *Nat. Mater.* **9** 230
- [73] Pai C-F, Nguyen M-H, Belvin C, Vilela-Leão L H, Ralph D and Buhrman R 2014 Enhancement of perpendicular magnetic anisotropy and transmission of spin-Hall-effect-induced spin currents by a Hf spacer layer in W/Hf/CoFeB/MgO layer structures *Appl. Phys. Lett.* **104** 082407
- [74] Nguyen M-H, Pai C-F, Nguyen K X, Muller D A, Ralph D and Buhrman R 2015 Enhancement of the anti-damping spin torque efficacy of platinum by interface modification *Appl. Phys. Lett.* **106** 222402
- [75] Qiu X, Deorani P, Narayanapillai K, Lee K-S, Lee K-J, Lee H-W and Yang H 2014 Angular and temperature dependence of current induced spin-orbit effective fields in Ta/CoFeB/MgO nanowires *Sci. Rep.* **4** 4491
- [76] Deorani P and Yang H 2013 Role of spin mixing conductance in spin pumping: Enhancement of spin pumping efficiency in Ta/Cu/Py structures *Appl. Phys. Lett.* **103** 232408
- [77] Hahn C, De Loubens G, Klein O, Viret M, Naletov V V and Youssef J B 2013 Comparative measurements of inverse spin Hall effects and magnetoresistance in YIG/Pt and YIG/Ta *Phys. Rev. B* **87** 174417
- [78] Pham V T, Vila L, Zahnd G, Marty A, Savero-Torres W, Jamet M and Attané J-P 2016 Ferromagnetic/nonmagnetic nanostructures for the electrical measurement of the Spin Hall effect *Nano Lett.* **16** 6755-60
- [79] Rojas-Sánchez J-C, Reyren N, Laczkowski P, Savero W, Attané J-P, Deranlot C, Jamet M, George J-M, Vila L and Jaffrès H 2014 Spin pumping and inverse spin Hall effect in platinum: the essential role of spin-memory loss at metallic interfaces *Phys. Rev. Lett.* **112** 106602
- [80] Zhang W, Han W, Jiang X, Yang S-H and Parkin S S 2015 Role of transparency of platinum-ferromagnet interfaces in determining the intrinsic magnitude of the spin Hall effect *Nat. Phys.* **11** 496-502
- [81] Pai C-F, Ou Y, Vilela-Leão L H, Ralph D and Buhrman R 2015 Dependence of the efficiency of spin Hall torque on the transparency of Pt/ferromagnetic layer interfaces *Phys. Rev. B* **92** 064426
- [82] Berger A J, Edwards E R, Nembach H T, Karis O, Weiler M and Silva T 2017 Determination of spin Hall effect and spin diffusion length of Pt from self-consistent fitting of damping enhancement and inverse spin-orbit torque measurements *arXiv preprint arXiv:1711.07654*
- [83] Zhang C, Yamanouchi M, Sato H, Fukami S, Ikeda S, Matsukura F and Ohno H 2013 Magnetotransport measurements of current induced effective fields in Ta/CoFeB/MgO *Appl. Phys. Lett.* **103** 262407
- [84] Wang H, Du C, Pu Y, Adur R, Hammel P C and Yang F 2014 Scaling of spin Hall angle in 3d, 4d, and 5d metals from Y 3 Fe 5 O 12/metal spin pumping *Phys. Rev. Lett.* **112** 197201

- [85] Qu D, Huang S, Miao B, Huang S and Chien C 2014 Self-consistent determination of spin Hall angles in selected 5 d metals by thermal spin injection *Phys. Rev. B* **89** 140407
- [86] Gómez J, Tedlla B Z, Álvarez N, Alejandro G, Goovaerts E and Butera A 2014 Spin transport parameters in Ni₈₀Fe₂₀/Ru and Ni₈₀Fe₂₀/Ta bilayers *Phys. Rev. B* **90** 184401
- [87] Liu J, Ohkubo T, Mitani S, Hono K and Hayashi M 2015 Correlation between the spin Hall angle and the structural phases of early 5 d transition metals *Appl. Phys. Lett.* **107** 232408
- [88] Kondou K, Sukegawa H, Kasai S, Mitani S, Niimi Y and Otani Y 2016 Influence of inverse spin Hall effect in spin-torque ferromagnetic resonance measurements *Appl. Phys. Express* **9** 023002
- [89] Kim J, Sheng P, Takahashi S, Mitani S and Hayashi M 2016 Spin Hall magnetoresistance in metallic bilayers *Phys. Rev. Lett.* **116** 097201
- [90] Hao Q and Xiao G 2015 Giant spin Hall effect and switching induced by spin-transfer torque in a W/Co₄₀Fe₄₀B₂₀/MgO structure with perpendicular magnetic anisotropy *Phys. Rev. Applied* **3** 034009
- [91] Cho S, Baek S-h C, Lee K-D, Jo Y and Park B-G 2015 Large spin Hall magnetoresistance and its correlation to the spin-orbit torque in W/CoFeB/MgO structures *Sci. Rep.* **5** 14668
- [92] Yu J, Qiu X, Legrand W and Yang H 2016 Large spin-orbit torques in Pt/Co-Ni/W heterostructures *Appl. Phys. Lett.* **109** 042403
- [93] Gabor M, Petrisor Jr T, Mos R, Mesaros A, Nasui M, Belmeguenai M, Zighem F and Tiusan C 2016 Spin-orbit torques and magnetization switching in W/Co₂FeAl/MgO structures *J. Phys. D: Appl. Phys.* **49** 365003
- [94] Niimi Y, Morota M, Wei D H, Deranlot C, Basletic M, Hamzic A, Fert A and Otani Y 2011 Extrinsic Spin Hall Effect Induced by Iridium Impurities in Copper *Phys. Rev. Lett.* **106** 126601
- [95] Niimi Y, Kawanishi Y, Wei D H, Deranlot C, Yang H X, Chshiev M, Valet T, Fert A and Otani Y 2012 Giant Spin Hall Effect Induced by Skew Scattering from Bismuth Impurities inside Thin Film CuBi Alloys *Phys. Rev. Lett.* **109** 156602
- [96] Niimi Y, Suzuki H, Kawanishi Y, Omori Y, Valet T, Fert A and Otani Y 2014 Extrinsic spin Hall effects measured with lateral spin valve structures *Phys. Rev. B* **89** 054401
- [97] Ramaswamy R, Wang Y, Elyasi M, Motapothula M, Venkatesan T, Qiu X and Yang H 2017 Extrinsic Spin Hall Effect in Cu_{1-x}Pt_x *Phys. Rev. Applied* **8** 024034
- [98] Niimi Y and Otani Y 2015 Reciprocal spin Hall effects in conductors with strong spin-orbit coupling: a review *Rep. Prog. Phys.* **78** 124501
- [99] Tian Y, Ye L and Jin X 2009 Proper scaling of the anomalous Hall effect *Phys. Rev. Lett.* **103** 087206
- [100] Fert A and Levy P M 2011 Spin Hall effect induced by resonant scattering on impurities in metals *Phys. Rev. Lett.* **106** 157208
- [101] Asomoza R, Fert A and Reich R 1983 Gadolinium-heavy rare earth alloys: preparation, metallographic study and extraordinary hall effect *J. Less Common Metals* **90** 177-201
- [102] Tokaç M, Bunyaev S, Kakazei G, Schmool D, Atkinson D and Hindmarch A 2015 Interfacial structure dependent spin mixing conductance in cobalt thin films *Phys. Rev. Lett.* **115** 056601
- [103] Perez N, Martinez E, Torres L, Woo S-H, Emori S and Beach G 2014 Chiral magnetization textures stabilized by the Dzyaloshinskii-Moriya interaction during spin-orbit torque switching *Appl. Phys. Lett.* **104** 092403
- [104] Zhang C, Fukami S, Sato H, Matsukura F and Ohno H 2015 Spin-orbit torque induced magnetization switching in nano-scale Ta/CoFeB/MgO *Appl. Phys. Lett.* **107** 012401
- [105] Fukami S, Anekawa T, Zhang C and Ohno H 2016 A spin-orbit torque switching scheme with collinear magnetic easy axis and current configuration *Nat. Nanotech.* **11** 621-5
- [106] Legrand W, Ramaswamy R, Mishra R and Yang H 2015 Coherent subnanosecond switching of perpendicular magnetization by the fieldlike spin-orbit torque without an external magnetic field *Physical Review Applied* **3** 064012
- [107] Lee O, Liu L, Pai C, Li Y, Tseng H, Gowtham P, Park J, Ralph D and Buhrman R A 2014 Central role of

- domain wall depinning for perpendicular magnetization switching driven by spin torque from the spin Hall effect *Phys. Rev. B* **89** 024418
- [108] Zhang C, Fukami S, DuttaGupta S, Sato H and Ohno H 2018 Time and spatial evolution of spin-orbit torque-induced magnetization switching in W/CoFeB/MgO structures with various sizes *Jpn. J. Appl. Phys* **57** 04FN2
- [109] König M, Wiedmann S, Brüne C, Roth A, Buhmann H, Molenkamp L W, Qi X-L and Zhang S-C 2007 Quantum spin Hall insulator state in HgTe quantum wells *Science* **318** 766-70
- [110] Xia Y, Qian D, Hsieh D, Wray L, Pal A, Lin H, Bansil A, Grauer D, Hor Y S, Cava R J and Hasan M Z 2009 Observation of a large-gap topological-insulator class with a single Dirac cone on the surface *Nat. Phys.* **5** 398-402
- [111] Zhang H, Liu C-X, Qi X-L, Dai X, Fang Z and Zhang S-C 2009 Topological insulators in Bi₂Se₃, Bi₂Te₃ and Sb₂Te₃ with a single Dirac cone on the surface *Nat. Phys.* **5** 438
- [112] Chen Y, Analytis J G, Chu J-H, Liu Z, Mo S-K, Qi X-L, Zhang H, Lu D, Dai X and Fang Z 2009 Experimental realization of a three-dimensional topological insulator, Bi₂Te₃ *science* **325** 178-81
- [113] Bernevig B A, Hughes T L and Zhang S-C 2006 Quantum spin Hall effect and topological phase transition in HgTe quantum wells *Science* **314** 1757-61
- [114] Hsieh D, Qian D, Wray L, Xia Y, Hor Y S, Cava R J and Hasan M Z 2008 A topological Dirac insulator in a quantum spin Hall phase *Nature* **452** 970
- [115] Moore J E 2010 The birth of topological insulators *Nature* **464** 194-8
- [116] Hasan M Z and Kane C L 2010 Colloquium: Topological insulators *Rev. Mod. Phys.* **82** 3045-67
- [117] Qi X-L and Zhang S-C 2011 Topological insulators and superconductors *Rev. Mod. Phys.* **83** 1057-110
- [118] Shiomi Y, Nomura K, Kajiwara Y, Eto K, Novak M, Segawa K, Ando Y and Saitoh E 2014 Spin-electricity conversion induced by spin injection into topological insulators *Phys. Rev. Lett.* **113** 196601
- [119] Fan Y, Upadhyaya P, Kou X, Lang M, Takei S, Wang Z, Tang J, He L, Chang L-T and Montazeri M 2014 Magnetization switching through giant spin-orbit torque in a magnetically doped topological insulator heterostructure *Nat. Mater.* **13** 699-704
- [120] Kondou K, Yoshimi R, Tsukazaki A, Fukuma Y, Matsuno J, Takahashi K S, Kawasaki M, Tokura Y and Otani Y 2016 Fermi-level-dependent charge-to-spin current conversion by Dirac surface states of topological insulators *Nat. Phys.* **12** 1027-31
- [121] Deorani P, Son J, Banerjee K, Koirala N, Brahlek M, Oh S and Yang H 2014 Observation of inverse spin Hall effect in bismuth selenide *Phys. Rev. B* **90** 094403
- [122] Fan Y and Wang K L 2016 Spintronics Based on Topological Insulators *Spin* **6** 1640001
- [123] Wang H, Kally J, Lee J S, Liu T, Chang H, Hickey D R, Mkhoyan K A, Wu M, Richardella A and Samarth N 2016 Surface-State-Dominated Spin-Charge Current Conversion in Topological-Insulator-Ferromagnetic-Insulator Heterostructures *Phys. Rev. Lett.* **117** 076601
- [124] Jamali M, Lee J S, Jeong J S, Mahfouzi F, Lv Y, Zhao Z, Nikolić B K, Mkhoyan K A, Samarth N and Wang J-P 2015 Giant Spin Pumping and Inverse Spin Hall Effect in the Presence of Surface and Bulk Spin-Orbit Coupling of Topological Insulator Bi₂Se₃ *Nano Lett.* **15** 7126-32
- [125] Liu L, Richardella A, Garate I, Zhu Y, Samarth N and Chen C-T 2015 Spin-polarized tunneling study of spin-momentum locking in topological insulators *Phys. Rev. B* **91** 235437
- [126] Lee J S, Richardella A, Hickey D R, Mkhoyan K A and Samarth N 2015 Mapping the chemical potential dependence of current-induced spin polarization in a topological insulator *Phys. Rev. B* **92** 155312
- [127] Kim J, Sinha J, Mitani S, Hayashi M, Takahashi S, Maekawa S, Yamanouchi M and Ohno H 2014 Anomalous temperature dependence of current-induced torques in CoFeB/MgO heterostructures with Ta-based underlayers *Phys. Rev. B* **89** 174424
- [128] Eldridge P, Leyland W, Lagoudakis P, Karimov O, Henini M, Taylor D, Phillips R and Harley R 2008 All-optical measurement of Rashba coefficient in quantum wells *Phys. Rev. B* **77** 125344
- [129] Fu L 2009 Hexagonal warping effects in the surface states of the topological insulator Bi₂Te₃ *Phys.*

- Rev. Lett.* **103** 266801
- [130] Wang Y H, Hsieh D, Pilon D, Fu L, Gardner D R, Lee Y S and Gedik N 2011 Observation of a Warped Helical Spin Texture in Bi_2Se_3 from Circular Dichroism Angle-Resolved Photoemission Spectroscopy *Phys. Rev. Lett.* **107** 207602
- [131] Nomura M, Souma S, Takayama A, Sato T, Takahashi T, Eto K, Segawa K and Ando Y 2014 Relationship between Fermi surface warping and out-of-plane spin polarization in topological insulators: A view from spin-and angle-resolved photoemission *Phys. Rev. B* **89** 045134
- [132] Kuroda K, Arita M, Miyamoto K, Ye M, Jiang J, Kimura A, Krasovskii E E, Chulkov E V, Iwasawa H, Okuda T, Shimada K, Ueda Y, Namatame H and Taniguchi M 2010 Hexagonally Deformed Fermi Surface of the 3D Topological Insulator Bi_2Se_3 *Phys. Rev. Lett.* **105** 076802
- [133] Xu Z, Guo X, Yao M, He H, Miao L, Jiao L, Liu H, Wang J, Qian D and Jia J 2013 Anisotropic Topological Surface States on High - Index Bi_2Se_3 Films *Adv. Mater.* **25** 1557-62
- [134] Yazyev O V, Moore J E and Louie S G 2010 Spin polarization and transport of surface states in the topological insulators Bi_2Se_3 and Bi_2Te_3 from first principles *Phys. Rev. Lett.* **105** 266806
- [135] MacNeill D, Stiehl G M, Guimaraes M H D, Buhrman R A, Park J and Ralph D C 2016 Control of spin-orbit torques through crystal symmetry in WTe_2 /ferromagnet bilayers *Nat. Phys.* **13** 300
- [136] Han J, Richardella A, Siddiqui S A, Finley J, Samarth N and Liu L 2017 Room-Temperature Spin-Orbit Torque Switching Induced by a Topological Insulator *Phys. Rev. Lett.* **119** 077702
- [137] Jamali M, Chen J-Y, Hickey D R, Zhang D, Zhao Z, Li H, Quarterman P, Lv Y, Li M and Mkhoyan K A 2017 Room-temperature perpendicular magnetization switching through giant spin-orbit torque from sputtered $\text{Bi}_x\text{Se}_{1-x}$ topological insulator material *arXiv preprint arXiv:1703.03822*
- [138] Bychkov Y A and Rashba E 1984 Properties of a 2D electron gas with lifted spectral degeneracy *JETP lett* **39** 78
- [139] Manchon A, Koo H C, Nitta J, Frolov S M and Duine R A 2015 New perspectives for Rashba spin-orbit coupling *Nat. Mater.* **14** 871
- [140] Koroteev Y M, Bihlmayer G, Gayone J, Chulkov E, Blügel S, Echenique P M and Hofmann P 2004 Strong spin-orbit splitting on Bi surfaces *Phys. Rev. Lett.* **93** 046403
- [141] Ast C R, Henk J, Ernst A, Moeschini L, Falub M C, Pacilé D, Bruno P, Kern K and Grioni M 2007 Giant spin splitting through surface alloying *Phys. Rev. Lett.* **98** 186807
- [142] Meier F, Dil H, Lobo-Checa J, Patthey L and Osterwalder J 2008 Quantitative vectorial spin analysis in angle-resolved photoemission: Bi / Ag (111) and Pb / Ag (111) *Phys. Rev. B* **77** 165431
- [143] Sánchez J R, Vila L, Desfonds G, Gambarelli S, Attané J, De Teresa J, Magén C and Fert A 2013 Spin-to-charge conversion using Rashba coupling at the interface between non-magnetic materials *Nat. Commun.* **4** 2944
- [144] Nomura A, Tashiro T, Nakayama H and Ando K 2015 Temperature dependence of inverse Rashba-Edelstein effect at metallic interface *Appl. Phys. Lett.* **106** 212403
- [145] Zhang W, Jungfleisch M B, Jiang W, Pearson J E and Hoffmann A 2015 Spin pumping and inverse Rashba-Edelstein effect in NiFe/Ag/Bi and NiFe/Ag/Sb *J. Appl. Phys.* **117** 17C727
- [146] Zhang H, Yamamoto S, Gu B, Li H, Maekawa M, Fukaya Y and Kawasuso A 2015 Charge-to-spin conversion and spin diffusion in Bi/Ag bilayers observed by spin-polarized positron beam *Phys. Rev. Lett.* **114** 166602
- [147] Jungfleisch M, Zhang W, Sklenar J, Jiang W, Pearson J, Ketterson J and Hoffmann A 2016 Interface-driven spin-torque ferromagnetic resonance by Rashba coupling at the interface between nonmagnetic materials *Phys. Rev. B* **93** 224419
- [148] Shi S, Wang A, Wang Y, Ramaswamy R, Shen L, Moon J, Zhu D, Yu J, Oh S, Feng Y and Yang H 2018 Efficient Charge-Spin Conversion and Magnetization Switching through Rashba Effect at Topological Insulator/Ag Interface *Phys. Rev. B* **97** 041115 (R)

- [149] Manzeli S, Ovchinnikov D, Pasquier D, Yazyev O V and Kis A 2017 2D transition metal dichalcogenides *Nat. Rev. Mater.* **2** 17033
- [150] Shao Q, Yu G, Lan Y-W, Shi Y, Li M-Y, Zheng C, Zhu X, Li L-J, Amiri P K and Wang K L 2016 Strong Rashba-Edelstein Effect-Induced Spin–Orbit Torques in Monolayer Transition Metal Dichalcogenide/Ferromagnet Bilayers *Nano Lett.* **16** 7514-20
- [151] Zhang W, Sklenar J, Hsu B, Jiang W, Jungfleisch M B, Xiao J, Fradin F Y, Liu Y, Pearson J E and Ketterson J B 2016 Research Update: Spin transfer torques in permalloy on monolayer MoS₂ *APL Mater.* **4** 032302
- [152] Sklenar J, Zhang W, Jungfleisch M B, Jiang W, Saglam H, Pearson J E, Ketterson J B and Hoffmann A 2016 Perspective: Interface generation of spin-orbit torques *J. Appl. Phys.* **120** 180901
- [153] MacNeill D, Stiehl G M, Guimarães M H, Reynolds N D, Buhrman R A and Ralph D C 2017 Thickness dependence of spin-orbit torques generated by WTe₂ *Phys. Rev. B* **96** 054450
- [154] Ali M N, Xiong J, Flynn S, Tao J, Gibson Q D, Schoop L M, Liang T, Haldolaarachchige N, Hirschberger M and Ong N 2014 Large, non-saturating magnetoresistance in WTe₂ *Nature* **514** 205-8
- [155] Jiang J, Tang F, Pan X, Liu H, Niu X, Wang Y, Xu D, Yang H, Xie B and Song F 2015 Signature of strong spin-orbital coupling in the large nonsaturating magnetoresistance material WTe₂ *Phys. Rev. Lett.* **115** 166601
- [156] Soluyanov A A, Gresch D, Wang Z, Wu Q, Troyer M, Dai X and Bernevig B A 2015 Type-II Weyl semimetals *Nature* **527** 495
- [157] Wadley P, Howells B, Železný J, Andrews C, Hills V, Campion R P, Novák V, Olejník K, Maccherozzi F and Dhesi S 2016 Electrical switching of an antiferromagnet *Science* **351** 587-90
- [158] Yang Y, Xu Y, Zhang X, Wang Y, Zhang S, Li R-W, Mirshekarloo M S, Yao K and Wu Y 2016 Fieldlike spin-orbit torque in ultrathin polycrystalline FeMn films *Phys. Rev. B* **93** 094402
- [159] Tsai M-H, Lin P-H, Huang K-F, Lin H-H and Lai C-H 2017 Spin-orbit-torque MRAM: from uniaxial to unidirectional switching *arXiv preprint arXiv:1706.01639*
- [160] Fukami S, Zhang C, DuttaGupta S, Kurenkov A and Ohno H 2016 Magnetization switching by spin-orbit torque in an antiferromagnet-ferromagnet bilayer system *Nat. Mater.* **15** 535-41
- [161] van den Brink A, Vermijs G, Solignac A, Koo J, Kohlhepp J T, Swagten H J M and Koopmans B 2016 Field-free magnetization reversal by spin-Hall effect and exchange bias *Nat. Commun.* **7** 10854
- [162] Lau Y-C, Betto D, Rode K, Coey J M D and Stamenov P 2016 Spin–orbit torque switching without an external field using interlayer exchange coupling *Nat. Nanotech.* **11** 758
- [163] Oh Y-W, Baek S-h C, Kim Y, Lee H Y, Lee K-D, Yang C-G, Park E-S, Lee K-S, Kim K-W and Go G 2016 Field-free switching of perpendicular magnetization through spin–orbit torque in antiferromagnet/ferromagnet/oxide structures *Nature nanotechnology* **11** 878-84
- [164] Sklenar J, Zhang W, Jungfleisch M B, Jiang W, Saglam H, Pearson J E, Ketterson J B and Hoffmann A 2016 Spin Hall effects in metallic antiferromagnets—perspectives for future spin-orbitronics *AIP Adv.* **6** 055603
- [165] Zhang W, Han W, Yang S-H, Sun Y, Zhang Y, Yan B and Parkin S S 2016 Giant facet-dependent spin-orbit torque and spin Hall conductivity in the triangular antiferromagnet IrMn₃ *Sci. Adv.* **2** e1600759
- [166] Mendes J, Cunha R, Santos O A, Ribeiro P, Machado F, Rodríguez-Suárez R, Azevedo A and Rezende S 2014 Large inverse spin Hall effect in the antiferromagnetic metal Ir₂₀Mn₈₀ *Phys. Rev. B* **89** 140406
- [167] Zhang W, Jungfleisch M B, Jiang W, Pearson J E, Hoffmann A, Freimuth F and Mokrousov Y 2014 Spin Hall effects in metallic antiferromagnets *Phys. Rev. Lett.* **113** 196602
- [168] Hwang H Y, Iwasa Y, Kawasaki M, Keimer B, Nagaosa N and Tokura Y 2012 Emergent phenomena at oxide interfaces *Nat. Mater.* **11** 103
- [169] Reyren N, Thiel S, Caviglia A, Kourkoutis L F, Hammerl G, Richter C, Schneider C, Kopp T, Rüetschi A-S and Jaccard D 2007 Superconducting interfaces between insulating oxides *Science* **317** 1196-9
- [170] Caviglia A, Gariglio S, Reyren N, Jaccard D, Schneider T, Gabay M, Thiel S, Hammerl G, Mannhart J

- and Triscone J-M 2008 Electric field control of the LaAlO₃/SrTiO₃ interface ground state *Nature* **456** 624
- [171] Brinkman A, Huijben M, Van Zalk M, Huijben J, Zeitler U, Maan J, van der Wiel W G, Rijnders G, Blank D H and Hilgenkamp H 2007 Magnetic effects at the interface between non-magnetic oxides *Nat. Mater.* **6** 493
- [172] Kalisky B, Bert J A, Klopfer B B, Bell C, Sato H K, Hosoda M, Hikita Y, Hwang H Y and Moler K A 2012 Critical thickness for ferromagnetism in LaAlO₃/SrTiO₃ heterostructures *Nat. Commun.* **3** 922
- [173] Lee J-S, Xie Y, Sato H, Bell C, Hikita Y, Hwang H and Kao C-C 2013 Titanium d xy ferromagnetism at the LaAlO₃/SrTiO₃ interface *Nat. Mater.* **12** 703
- [174] Ohtomo A and Hwang H Y 2004 A high-mobility electron gas at the LaAlO₃/SrTiO₃ heterointerface *Nature* **427** 423-6
- [175] Caviglia A, Gabay M, Gariglio S, Reyren N, Cancellieri C and Triscone J-M 2010 Tunable Rashba spin-orbit interaction at oxide interfaces *Phys. Rev. Lett.* **104** 126803
- [176] Joshua A, Pecker S, Ruhman J, Altman E and Ilani S 2012 A universal critical density underlying the physics of electrons at the LaAlO₃/SrTiO₃ interface *Nat. Commun.* **3** 2116
- [177] Zhong Z, Tóth A and Held K 2013 Theory of spin-orbit coupling at LaAlO₃/SrTiO₃ interfaces and SrTiO₃ surfaces *Phys. Rev. B* **87** 161102
- [178] Edelstein V M 1990 Spin polarization of conduction electrons induced by electric current in two-dimensional asymmetric electron systems *Solid State Commun.* **73** 233-5
- [179] Narayanapillai K, Gopinadhan K, Qiu X, Annadi A, Ariando, Venkatesan T and Yang H 2014 Current-driven spin orbit field in LaAlO₃/SrTiO₃ heterostructures *Appl. Phys. Lett.* **105** 162405
- [180] Wang Y, Ramaswamy R, Motapothula M, Narayanapillai K, Zhu D, Yu J, Venkatesan T and Yang H 2017 Room Temperature Giant Charge-to-Spin Conversion at SrTiO₃/LaAlO₃ Oxide Interface *Nano Lett.* **17** 7659
- [181] Lesne E, Fu Y, Oyarzun S, Rojas-Sanchez J C, Vaz D C, Naganuma H, Sicoli G, Attane J P, Jamet M, Jacquet E, George J M, Barthelemy A, Jaffres H, Fert A, Bibes M and Vila L 2016 Highly efficient and tunable spin-to-charge conversion through Rashba coupling at oxide interfaces *Nat Mater* **15** 1261-6
- [182] Chauleau J-Y, Boselli M, Gariglio S, Weil R, De Loubens G, Triscone J-M and Viret M 2016 Efficient spin-to-charge conversion in the 2D electron liquid at the LAO/STO interface *EPL* **116** 17006
- [183] Song Q, Zhang H, Su T, Yuan W, Chen Y, Xing W, Shi J, Sun J and Han W 2017 Observation of inverse Edelstein effect in Rashba-split 2DEG between SrTiO₃ and LaAlO₃ at room temperature *Sci. Adv.* **3** e1602312
- [184] Jin M-J, Moon S Y, Park J, Modepalli V, Jo J, Kim S-I, Koo H C, Min B-C, Lee H-W and Baek S-H 2016 Nonlocal Spin Diffusion Driven by Giant Spin Hall Effect at Oxide Heterointerfaces *Nano Lett.* **17** 36-43
- [185] Ohshima R, Ando Y, Matsuzaki K, Susaki T, Weiler M, Klingler S, Huebl H, Shikoh E, Shinjo T and Goennenwein S T 2017 Strong evidence for d-electron spin transport at room temperature at a LaAlO₃/SrTiO₃ interface *Nat. Mater.* **16** 609–14
- [186] Demasius K-U, Phung T, Zhang W, Hughes B P, Yang S-H, Kellock A, Han W, Pushp A and Parkin S S 2016 Enhanced spin-orbit torques by oxygen incorporation in tungsten films *Nat. Commun.* **7** 10644
- [187] An H, Kageyama Y, Kanno Y, Enishi N and Ando K 2016 Spin-torque generator engineered by natural oxidation of Cu *Nat. Commun.* **7** 13069
- [188] Qiu X, Narayanapillai K, Wu Y, Deorani P, Yang D-H, Noh W-S, Park J-H, Lee K-J, Lee H-W and Yang H 2015 Spin-orbit-torque engineering via oxygen manipulation *Nat. Nanotech.* **10** 333-8
- [189] Garello K, Avci C O, Miron I M, Baumgartner M, Ghosh A, Auffret S, Boulle O, Gaudin G and Gambardella P 2014 Ultrafast magnetization switching by spin-orbit torques *Appl. Phys. Lett.* **105** 212402

- [190] Yoon J, Lee S-W, Kwon J H, Lee J M, Son J, Qiu X, Lee K-J and Yang H 2017 Anomalous spin-orbit torque switching due to field-like torque–assisted domain wall reflection *Sci. Adv.* **3** e1603099
- [191] Shi S, Ou Y, Aradhya S, Ralph D and Buhrman R 2018 Fast Low-Current Spin-Orbit-Torque Switching of Magnetic Tunnel Junctions through Atomic Modifications of the Free-Layer Interfaces *Phys. Rev. Applied* **9** 011002
- [192] Lee J M, Kwon J H, Ramaswamy R, Yoon J, Son J, Qiu X, Mishra R, Srivastava S, Cai K and Yang H 2018 Oscillatory spin-orbit torque switching induced by field-like torques *Communications Physics* **1** 2
- [193] Amiri P K, Zeng Z, Upadhyaya P, Rowlands G, Zhao H, Krivorotov I, Wang J-P, Jiang H, Katine J, Langer J, Galatsis K and Wang K L 2011 Low write-energy magnetic tunnel junctions for high-speed spin-transfer-torque MRAM *IEEE Electron Device Letters* **32** 57-9
- [194] Chen E, Apalkov D, Driskill-Smith A, Khvalkovskiy A, Lottis D, Moon K, Nikitin V, Ong A, Tang X and Watts S 2012 Progress and prospects of spin transfer torque random access memory *IEEE Trans. Magn.* **48** 3025-30
- [195] Cai H, Kang W, Wang Y, Naviner L A D B, Yang J and Zhao W 2017 High Performance MRAM with Spin-Transfer-Torque and Voltage-Controlled Magnetic Anisotropy Effects *Applied Sciences* **7** 929
- [196] Harder M, Gui Y and Hu C-M 2016 Electrical detection of magnetization dynamics via spin rectification effects *Phys. Rep.* **661** 1-59
- [197] Chiba T, Bauer G E and Takahashi S 2014 Current-Induced Spin-Torque Resonance of Magnetic Insulators *Phys. Rev. Applied* **2** 034003
- [198] Schreier M, Chiba T, Niedermayr A, Lotze J, Huebl H, Geprägs S, Takahashi S, Bauer G E W, Gross R and Goennenwein S T B 2015 Current-induced spin torque resonance of a magnetic insulator *Phys. Rev. B* **92** 144411
- [199] Wang P, Jiang S, Luan Z, Zhou L, Ding H, Zhou Y, Tao X and Wu D 2016 Spin rectification induced by spin Hall magnetoresistance at room temperature *Appl. Phys. Lett.* **109** 112406
- [200] Wang Z, Gresch D, Soluyanov A A, Xie W, Kushwaha S, Dai X, Troyer M, Cava R J and Bernevig B A 2016 MoTe₂: a type-II Weyl topological metal *Phys. Rev. Lett.* **117** 056805
- [201] Núñez A S, Duine R, Haney P and MacDonald A 2006 Theory of spin torques and giant magnetoresistance in antiferromagnetic metals *Phys. Rev. B* **73** 214426
- [202] Haney P M and MacDonald A 2008 Current-induced torques due to compensated antiferromagnets *Phys. Rev. Lett.* **100** 196801
- [203] Mishra R, Yu J, Qiu X, Motapothula M, Venkatesan T and Yang H 2017 Anomalous current-induced spin torques in ferrimagnets near compensation *Physical Review Letters* **118** 167201
- [204] Cheng X, Katine J, Rowlands G and Krivorotov I 2013 Nonlinear ferromagnetic resonance induced by spin torque in nanoscale magnetic tunnel junctions *Appl. Phys. Lett.* **103** 082402
- [205] Miwa S, Ishibashi S, Tomita H, Nozaki T, Tamura E, Ando K, Mizuochi N, Saruya T, Kubota H and Yakushiji K 2014 Highly sensitive nanoscale spin-torque diode *Nat. Mater.* **13** 50-6
- [206] Fang B, Carpentieri M, Hao X, Jiang H, Katine J A, Krivorotov I N, Ocker B, Langer J, Wang K L and Zhang B 2016 Giant spin-torque diode sensitivity in the absence of bias magnetic field *Nat. Commun.* **7** 11259